A New Approach to Steady-State Modeling, Analysis, and Design of Power Converters

Mohammad Daryaei, *Student Member, IEEE*, S. Ali Khajehoddin, *Senior Member, IEEE*,
Javad Mashreghi, and Khurram K. Afridi, *Senior Member, IEEE*

***Abstract*—Steady-state models of power converters that provide accurate closed-form expressions for converter waveforms are extremely valuable for converter analysis and design, and enable comparative evaluation of different converter topologies. An obstacle in the development of such models is the inherent nonlinearity of switching power converters. This article presents a systematic procedure to model a broad class of power converters using ordinary differential equations (ODEs) with periodic and discontinuous inputs, and provides an approach to determine closed-form expressions for their steady-state waveforms. The formal mathematical proof of the proposed approach to finding closed-form expressions for the steady-state solution of ODEs with periodic and discontinuous inputs, Laplace-based theorem (LBT), is also presented. The presented modeling procedure and LBT, collectively called Laplace-based steady-state modeling (LBSM), serves as an effective analysis and design tool for power converters. The value of LBSM is demonstrated by using it to obtain closed-form expressions for the steady-state waveforms of different types of converters. In particular, two commonly used topologies—the series resonant converter and the phase-shift converter—are analyzed and compared using LBSM and their optimum operating conditions and applications are discussed. The converter waveforms, soft switching ranges and other characteristics obtained using LBSM are also validated through simulations and experiments.**

***Index Terms*—Laplace transform, phase-shift converter, series resonant converter, steady-state modeling, switching power converters, symbolic analysis and design.**

I. INTRODUCTION

STEADY-STATE models of power converters that can accurately predict converter voltage and current waveforms are extremely valuable for converter analysis and design, as they enable determination of component voltage and current stresses, identification of soft-switching opportunities, loss estimation, component selection, and topology comparisons. The most valuable modeling techniques are those that provide accurate closed-form expressions for converter waveforms, as they also enable rapid design optimization [1], [2]. The main obstacle in determining accurate closed-form steady-state waveforms for switching power converters is the presence of switches that introduce nonlinearity into the circuit. The switching action of the switches can be mathematically modeled by discontinuous functions in the governing differential equation of the power converter. However, the presence of the discontinuous functions makes solving the converter's differential equation for a closed-form solution a serious challenge.

Various methods have been developed to determine the steady-state switched waveforms of power converters, including a variety of numerical and analytical techniques [3], [4]. The simplest numerical technique relies on computing the converter's state variables by integrating its state equations in small time-steps, starting with zero initial conditions, across multiple switching periods until the values of the state variables reach periodic steady state [5]. This approach is widely used and can be implemented using commercial circuit simulators, but is computationally inefficient [4]. More efficient numerical techniques have also been developed that determine the initial values of the state variables under steady-state operation before solving for the converter waveforms across only one switching period. These include iterative search techniques [6], [7], a noniterative augmented state-vector-based technique, which is limited to converters with known subinterval durations [8], and a hybrid approach, which combines the augmented state-vector technique with a binary search to make it broadly applicable [9]. However, unlike closed-form solutions, numerical approaches do not provide insights into the dependence of converter waveforms on its parameters, and are computationally less efficient during converter optimization.

A number of analytical modeling techniques have also been developed to determine steady-state waveforms. A popular analytical approach to converter modeling, applicable to both steady state and transient operation, is state-space averaging, in which an averaged circuit model and averaged state-space equations of the converter are developed by averaging its switching action over a switching period [10]. While extremely valuable for studying averaged converter dynamics of PWM converters operating in continuous conduction mode (CCM) and the design of their controllers, such averaged models cannot predict waveform dynamics within a switching period and cannot be directly used to determine switched waveforms [11].

Manuscript received October 20, 2020; revised January 22, 2021 and March 19, 2021; accepted April 13, 2021. Date of publication April 30, 2021; date of current version July 30, 2021. This work was supported by NSERC. Recommended for publication by Associate Editor H. Li. *(Corresponding author: Mohammad Daryaei.)*

Mohammad Daryaei and S. Ali Khajehoddin are with the Department of Electrical and Computer Engineering, University of Alberta, Edmonton, AB T6G 1H9, Canada (e-mail: daryayi@ualberta.ca; khajeddin@ieee.org).

Javad Mashreghi is with the Department of Mathematics and Statistics, Universite Laval, Québec, QC G1V 0A6, Canada (e-mail: javad.mashreghi@mat.ulaval.ca).

Khurram K. Afridi is with the School of Electrical and Computer Engineering, Cornell University, Ithaca, NY 14853 USA (e-mail: afridi@cornell.edu).

Color versions of one or more figures in this article are available at https://doi.org/10.1109/TPEL.2021.3076745.

Digital Object Identifier 10.1109/TPEL.2021.3076745

Approximate closed-form expressions for switched waveforms of PWM converters operating in CCM can be found by superimposing the ripple in the state variables, determined under small ripple approximation, onto their steady-state average values [10]. This approach does not work well for converters with large ripple, such as PWM converters operating in discontinuous conduction mode (DCM), soft-switching converters, and resonant converters. More sophisticated averaging techniques that attempt to capture the waveform dynamics within a switching period by incorporating switching frequency and higher order harmonics, in addition to the dc component, have also been developed [12]–[15]. The use of large number of harmonics to achieve high degree of accuracy makes these techniques cumbersome and does not yield closed-form expressions. The simplest of these approaches, widely used in the modeling of resonant converters, uses only the fundamental component of the switching waveform and is referred to as fundamental harmonic analysis (FHA) or sinusoidal analysis [16]. While this approach yields closed-form expressions, the results are accurate only for resonant converters with high loaded quality factor resonant tanks. Additional steady-state modeling approaches include analytically solving the differential equations associated with each switching interval of the converter and equating the state variable waveforms at the beginning and end of the switching period [17], [18]. A related approach is state plane analysis, in which state variable waveforms are mapped to geometric figures comprising segments of circles, lines, or ellipses [19], [20]. State plane analysis becomes extremely tedious for converters with more than two state variables, and both of the abovementioned time domain approaches require finding all the switching intervals of the converter and the initial values of the state variables, which is not straightforward. Another time domain steady-state modeling approach is step-superposition analysis, in which step responses to switch-network imposed steps are summed up by leveraging geometric series analysis to determine closed-form expressions for converter waveforms [21]. However, this approach has only been successfully demonstrated for converters in which the switch networks can be replaced by independent sources.

Recently a new approach to determine accurate closed-form steady-state solutions of ordinary differential equations (ODEs) with periodic and discontinuous input, referred to as Laplace-based theorem (LBT), has been introduced [22], and used to analyze a series resonant converter [23]. However, this approach can only be applied to a limited set of power converters, referred to here as edge switch-network converters, where the switching action of the converter's switches does not reconfigure the interconnection between its energy storage elements. This article presents a generalized technique, referred to as Laplace-based steady-state modeling (LBSM), which leverages LBT and introduces a systematic modeling procedure to model a broad class of power converters using ODEs with periodic and discontinuous inputs, including edge switch-network converters as well as interior switch-network converters, in which the switching action reconfigures the interconnection between its energy storage elements. To demonstrate the effectiveness of LBSM, this article uses LBSM to determine closed-form steady-state waveforms for a number of power converters, including the buck converter, the boost converter, the series resonant converter, and the phase-shift converter. LBSM is also leveraged to determine the zero voltage switching (ZVS) conditions for the series resonant converter and the phase-shift converter and compare these converters in terms of efficiency. It is shown that in applications where the variation in input voltage is less than a factor of two, the series resonant converter has superior performance; while in applications where the variation in input voltage is larger, the phase-shift converter has superior performance. This article also provides a rigorous proof of the LBT.

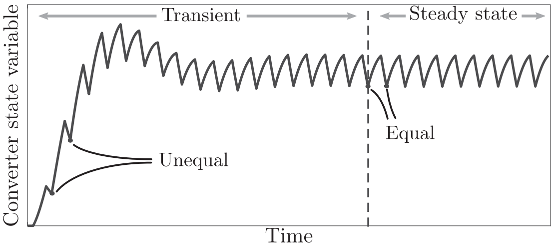

Fig. 1. Response of a power converter with an arbitrary initial condition, showing its state variable going through a transient before reaching steady state.

The remainder of this article is organized as follows. Section II presents the LBT and describes the procedure to finding the steady-state response of ODEs with inputs that are periodic discontinuous functions. The LBSM technique is described for edge and interior switch-network converters in Section III. To demonstrate the effectiveness of this technique for edge and interior switch-network converters, closed-form steady-state models for the buck converter and the boost converter are also developed using LBSM in Section III. The LBSM technique is utilized to analyze and design a phase-shift controlled series resonant converter and a phase-shift converter in Section IV. Section IV also compares these two converters. The predicted results for the series resonant converter and the phase-shift converter are experimentally validated in Section V. Finally, Section VI concludes this article. This article also has six appendices.

II. STEADY-STATE SOLUTION OF ODEs USING LBT

A power converter can be mathematically modeled by its governing differential equation(s) in which its switching actions are represented by periodic discontinuous functions. The mathematical model can be a single differential equation (typically of high order), or multiple first-order differential equations in the form of state-space representation. Here, the single differential equation approach is used for simplicity, and the state-space approach is presented in Appendix II. Determining an accurate closed-form expression for the steady-state response of the converter is not straight-forward, as with arbitrary initial conditions the converter's response will typically go through a transient before reaching steady state, as shown in Fig. 1. During the transient, the state variables of the converter (i.e., its capacitor voltages and inductor currents) have different values at the beginning and end of a switching period. On the other hand, in steady-state operation, the state variables have the same values at the beginning and end of the switching period and the waveform repeats itself. Therefore, the converter's steady-state waveform can be determined by solving its differential equation over one switching period provided the initial values of the state variable and its time derivatives under steady-state operation are known. These initial values can be determined using LBT, which is introduced next.

A. Laplace Based Theorem

LBT provides a method to determine the initial values for the steady-state solution of a constant-coefficient nonhomogeneous ordinary differential equation with periodic and discontinuous input. Consider a system with the constant-coefficient nonhomogeneous ordinary differential equation

$$a_n \frac{d^n x}{dt^n} + a_{n-1}\frac{d^{n-1}x}{dt^{n-1}} + \cdots + a_0 x(t) = f(t), \qquad (t > 0) \tag{1}$$

where x is the state variable, t is time, a_k's ($0 \leq k \leq n$ and $a_n \neq 0$) are constant coefficients (which in general can be complex), and the input f is a periodic function with period T that is integrable over $[0, \mathrm{T})$. The input f can be a linear combination of a piecewise smooth function with finite number of discontinuities and a finite number of Dirac functions on $[0, \mathrm{T})$. Taking the Laplace transform of (1) gives

$$P(s)X(s) + Q(s) = F(s) \tag{2}$$

where $P(s) = \sum_{k=1}^{n} a_k s^k$ is the differential equation's characteristic polynomial of order n, $X(s)$ is the Laplace transform of $x(t)$, $F(s) = (\int_0^{\mathrm{T}} f(t)e^{-st}dt)/(1 - e^{-s\mathrm{T}})$ is the Laplace transform of the periodic input function $f(t)$, and $Q(s)$ is a polynomial of degree at most $n - 1$ formed using the initial values of the system and given by

$$Q(s) = -x(0)a_n s^{n-1} - (x(0)a_{n-1} + x'(0)a_n)s^{n-2} - \cdots$$

$$= \begin{bmatrix} -x(0) \\ -x'(0) \\ \vdots \\ -x^{(n-1)}(0) \end{bmatrix}^T \begin{bmatrix} a_n & a_{n-1} & \cdots & a_2 & a_1 \\ 0 & a_n & & & a_2 \\ 0 & 0 & & & \vdots \\ \vdots & \vdots & & a_n & a_{n-1} \\ 0 & 0 & \cdots & 0 & a_n \end{bmatrix} \begin{bmatrix} s^{n-1} \\ s^{n-2} \\ \vdots \\ s \\ 1 \end{bmatrix} \tag{3}$$

where $x(0)$and $x'(0), \ldots, x^{(n-1)}(0)$ are the n unknown initial values of the state variable x and its time derivatives.

Assuming that $P(s)$ has n distinct roots $s_1, \ldots, s_n$ that do not intersect with the poles of $F(s)$, LBT states that the system has a periodic solution if and only if

$$\Big[Q(s_1), Q(s_2), \ldots, Q(s_n)\Big] = \Big[F(s_1), F(s_2), \ldots, F(s_n)\Big]. \tag{4}$$

A rigorous proof of LBT is provided in Appendix I.

B. ODE Steady-State Solution Using LBT

LBT can be leveraged to determine the initial values of the state variable under steady-state operation. Simply substituting (3) into (4) results in the n linear equations given by (5) at the bottom of the page, which can be used to find the n unknown initial values for the steady-state solution. Since the s_k's are distinct, the matrix $[s_k^{n-l}]_{1 \leq k, l \leq n}$ is invertible. Also, since $a_n \neq 0$, the upper triangular matrix is invertible. Hence, the equation given by (5) always has a unique solution for $x(0), \ldots, x^{(n-1)}(0)$. Therefore, the following procedure is proposed to determine the closed-form steady-state solution of a constant coefficient nonhomogeneous ODE having the form of (1).

S1) Determine $F(s) = \mathcal{L}\{f(t)\}$, where $f(t)$ is periodic with period T and can be discontinuous.

S2) Determine $s_1, s_2, \ldots, s_n$, the roots of the characteristic polynomial $P(s) = \sum_{k=1}^{n} a_k s^k$.

S3) Formulate the set of n linear equations in accordance with (5), and solve (5) to determine the n steady-state initial values $x(0), \ldots, x^{(n-1)}(0)$.

S4) Using the n initial steady-state values of the state variable and its time derivatives, solve (1) to find the steady-state solution for $x(t)$ across one switching period.

To understand the limitations of the proposed approach note that since LBT is based on a constant coefficient differential equation, it cannot be applied to power converters that contain nonlinear elements other than switches, such as saturable inductors and nonlinear capacitors. Also since there are no algebraic closed-form solutions for the roots of a general polynomial equation of degree five or higher, algebraic closed-form expressions for the waveforms of converters with more than four state variables are not guaranteed. However, closed-form expressions that include non-algebraic operations may exist for some of these cases. Other than these limitations, the proposed approach can be used for a broad class of power converters. The requirement that the roots of $P(s)$ have to be distinct from one another and different from the poles of $F(s)$ is rarely not met in real power converters. For example, if a root of $P(s)$ is at the same location as a pole of $F(s)$ then the converter will have an undamped oscillatory response, which is undesirable and will be intentionally avoided in a practical design. Also if $P(s)$ has nondistinct roots, this will occur for a specific

$$\begin{bmatrix} -x(0) \\ -x'(0) \\ \vdots \\ -x^{(n-1)}(0) \end{bmatrix}^T \begin{bmatrix} a_n & a_{n-1} & \cdots & a_2 & a_1 \\ 0 & a_n & & & a_2 \\ 0 & 0 & & & \vdots \\ \vdots & \vdots & & a_n & a_{n-1} \\ 0 & 0 & \cdots & 0 & a_n \end{bmatrix} \begin{bmatrix} s_1^{n-1} & s_2^{n-1} & \cdots & s_n^{n-1} \\ s_1^{n-2} & s_2^{n-2} & \cdots & s_n^{n-2} \\ \vdots & \vdots & & \vdots \\ 1 & 1 & \cdots & 1 \end{bmatrix} = \begin{bmatrix} F(s_1) \\ F(s_2) \\ \vdots \\ F(s_n) \end{bmatrix}^T \tag{5}$$

loading condition. For this rare case, converter waveforms can be obtained using a slightly different loading condition in the very close vicinity of the original loading without introducing much error in a practical design. It should also be noted that although LBT holds even when the ODE's constant coefficients (a_k's) are complex numbers, these coefficients will be real for a power converter comprising only switches and linear time invariant (LTI) elements.

III. LAPLACE BASED STEADY-STATE MODELING

LBT provides an approach to determine closed-form expressions for the steady-state solution of ODEs with periodic and discontinuous input. However, to utilize LBT to find a converter's steady-state waveforms, the converter must be modeled as a constant-coefficient ODE having the form of (1). Therefore, the LBSM approach introduced here has two high-level steps. In the first step, a constant coefficient ODE is derived that models the steady-state switched behavior of the converter. In the second step, the procedure described in Section II-B is applied to the converter's ODE to determine its steady-state waveforms.

Switching power converters comprise linear elements (capacitors, inductors, and transformers), also referred to as energy storage elements, and switches. Converters interface with sources and loads at their input and output ports. Depending on their topology, converters can be categorized into one of two classes: 1) edge switch-network converters, or 2) interior switch-network converters. If the switching action of the converter's switches does not reconfigure the interconnection between its energy storage elements, the converter is called an edge switch-network converter. This will typically only be possible when the switches are connected to the input and/or output ports of the converter. Examples of edge switch-network converters include buck converter, voltage source inverter, and series resonant converter (if the dynamics of its output filter are negligible). If the switching action of the converter's switches reconfigures the interconnection between its energy storage elements, the converter is called an interior switch-network converter. Examples of interior switch-network converters include boost converter, buck–boost converter, Cuk converter, SEPIC converter, Zeta converter, four-switch buck–boost converter, Watkins–Johnson converter, flyback converter, and any of the edge switch-network converters with an input filter whose dynamics cannot be ignored. Different procedures are needed to model edge and interior switch-network converters in the form of constant-coefficient ODEs.

A. Edge Switch-Network Converters

In edge switch-network converters, the voltage across, or the current through, each switch can be determined solely from the values of the actual or equivalent sources connected at the input and/or output ports of the converter. Hence, individual switches, or more commonly switch networks, can be replaced by time varying independent voltage or current sources, simplifying the derivation of its ODE. To model an edge switch-network converter in the form of an ODE, the following procedure is proposed.

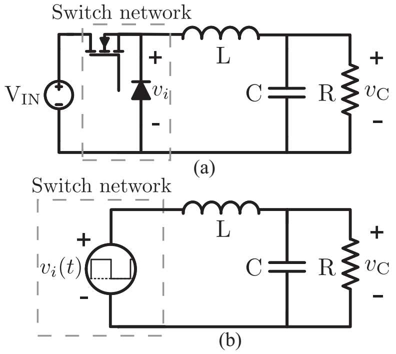

Fig. 2. Buck converter: (a) topology, and (b) switched-mode equivalent circuit model.

M1) Create an equivalent circuit model for the converter by replacing switch networks and/or individual switches with periodic discontinuous independent voltage or current sources that model the ports of the switch networks and/or the switches.

M2) Determine the converter's governing differential equation from the equivalent circuit model in terms of one of its state variables. This equation will be a constant coefficient ODE of the form of (1).

As an example, consider the buck converter shown in Fig. 2(a). This converter can be separated into two cascaded networks: a switch network and an energy storage network. The switch network comprises two switches (a MOSFET and a diode) and is connected to the input voltage source at the input port of the converter. The energy storage network comprises an inductor and a capacitor and is connected to a load resistor at the output port of the converter, forming a LTI network. Following step (M1) and assuming that the converter is operating in CCM, the voltage across the diode is either $\mathrm{V_{IN}}$ (when MOSFET is ON) or zero (when MOSFET is OFF). Hence, the buck converter can be modeled using the equivalent circuit shown in Fig. 2(b). Following step (M2), Fig. 2(b) can be used to easily determine the following constant coefficient ODE for the buck converter operating in CCM:

$$\mathrm{LC}\frac{d^2 v_\mathrm{C}}{dt^2} + \frac{\mathrm{L}}{\mathrm{R}}\frac{dv_\mathrm{C}}{dt} + v_\mathrm{C}(t) = v_i(t) \tag{6}$$

where $v_i(t) = q(t)\mathrm{V_{IN}}$, and $q(t)$ is a switching function which equals 1 when the MOSFET (i.e., active switch) is ON and 0 when the MOSFET is OFF.

The steady-state solution for this ODE can be found using the four steps given in Section II-B. Following step (S1), the Laplace transform of the input function is:

$$F(s) = \mathcal{L}\{v_i(t)\} = \mathrm{V_{IN}}\frac{1 - e^{-sD\mathrm{T_s}}}{s\left(1 - e^{-s\mathrm{T_s}}\right)} \tag{7}$$

where $\mathrm{T_s}$ is the switching period and D is the duty cycle of the converter. Next, following step (S2), the characteristic polynomial has the following roots:

$$s_{1,2} = \frac{1}{2\mathrm{RC}}\left(-1 \pm \sqrt{1 - 4\frac{\mathrm{R^2C}}{\mathrm{L}}}\right) \equiv s_r \pm s_m \tag{8}$$

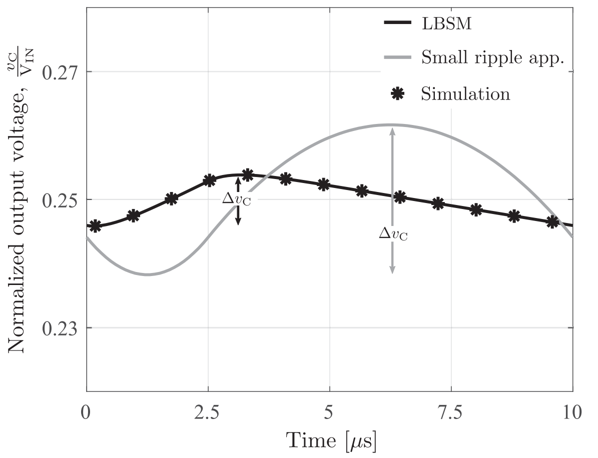

Fig. 3. Comparison of normalized output voltage waveform obtained using LBSM, numerical simulation, and small ripple approximation for a buck converter with following parameter values: $L = 20\,\mu H$, $C = 5\,\mu F$, $R = 0.1\,\Omega$, $D = 0.25$, and $f_s = 100$ kHz. Here, $\Delta v_C/V_C$ is 3.2% and 9.4% for the LBSM and small ripple approximation waveforms, respectively.

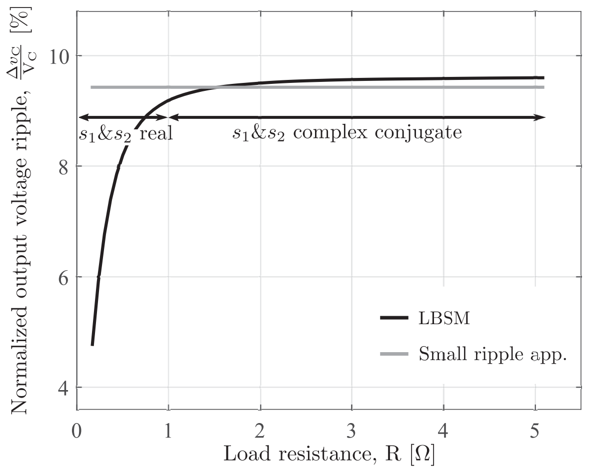

Fig. 4. Comparison of normalized peak-to-peak output voltage ripple $\frac{\Delta v_C}{v_C}$ as a function of load resistance obtained using LBSM and small ripple approximation for the example buck converter of Fig. 3.

Following step (S3), and formulating $Q(s_k) = F(s_k)$ for $k = 1, 2$ in the form of (5), results in the following set of linear equations:

$$-\begin{bmatrix} v_C(0) & v'_C(0) \end{bmatrix} \begin{bmatrix} LC & \frac{L}{R} \\ 0 & LC \end{bmatrix} \begin{bmatrix} s_1 & s_2 \\ 1 & 1 \end{bmatrix} = \begin{bmatrix} F(s_1) & F(s_2) \end{bmatrix} \tag{9}$$

which can be solved for the initial conditions $v_C(0)$ and $v'_C(0)$ to obtain

$$v_C(0) = \frac{F(s_1)-F(s_2)}{LC(s_2-s_1)},\; v'_C(0) = \frac{s_1F(s_1)-s_2F(s_2)}{LC(s_2-s_1)}. \tag{10}$$

Finally, following step (S4), and solving (6) across one switching period using the abovementioned initial conditions, yields the following output voltage:

$$v_C(t) = \begin{cases} e^{s_r t}\left(A\cosh(s_m t) + \frac{B}{s_m}\sinh(s_m t)\right) + V_{IN} & 0 < t \leq DT_s \\ e^{s_r t}\left(A'\cosh(s_m t) + \frac{B'}{s_m}\sinh(s_m t)\right) & DT_s < t \leq T_s \end{cases} \tag{11}$$

where $A = v_C(0) - V_{IN}$, $B = v'_C(0) - s_r(v_C(0) - V_{IN})$, $A' = A + V_{IN}e^{-s_r DT_s}(\cosh(s_m DT_s) + \frac{s_r}{s_m}\sinh(s_m DT_s))$, and $B' = B - V_{IN}e^{-s_r DT_s}(s_r\cosh(s_m DT_s) + s_m\sinh(s_m DT_s))$.

To validate the accuracy of the closed-form expression for the output voltage waveform given by (11), it is compared with a simulated steady-state waveform generated using PSIM in Fig. 3 for an example buck converter design. The LBSM and PSIM simulation results are identical, since they both accurately solve the same differential equation—the simulation software solves the differential equation numerically from period to period until it reaches steady state, while LBSM solves it analytically across only one period. Fig. 3 also plots the output voltage waveform of the buck converter obtained using small ripple approximation. The output voltage waveform, and the associated voltage ripple, predicted by small ripple approximation is quite different from the actual one predicted by numerical simulation and LBSM. Hence, the waveform obtained using LBSM can be used to analyze and design the buck converter more accurately than small ripple approximation. The values of normalized peak-to-peak output voltage ripple as predicted by LBSM and small ripple approximation are compared for a range of load resistances in Fig. 4. It is interesting to note that the output voltage ripple predicted by small ripple approximation is independent of load resistance (and equal to 9.4% in this example), while it depends on the load resistance according to LBSM. For small values of load resistance (where s_1 and s_2 in (8) are real), the output voltage ripple is substantially smaller than what is predicted by small ripple approximation. This makes sense as the output filter of the buck converter is highly damped under these conditions. Therefore, if the buck converter does not have to be operated under light loading, the LBSM-based design could prevent output capacitor over-design and result in improved power density of the converter.

In the abovementioned example, the buck converter is assumed to be operating in CCM, so the duration of each subinterval is known from the active switch's control signal. In cases where subinterval durations cannot be simply determined from switch control signals (e.g., buck converter operating in DCM), the subinterval durations will need to be included in LBSM as additional unknown variables, and their values determined by imposing appropriate constraints on the resulting waveform expressions. For example, in the case of a buck converter operating in DCM, the time at which the inductor current becomes zero can be defined as an unknown variable before applying LBSM. After the inductor current waveform has been determined using LBSM, its expression can be set equal to zero and solved for the unknown zero crossing time. The obtained equation is nonlinear, but can be solved numerically.

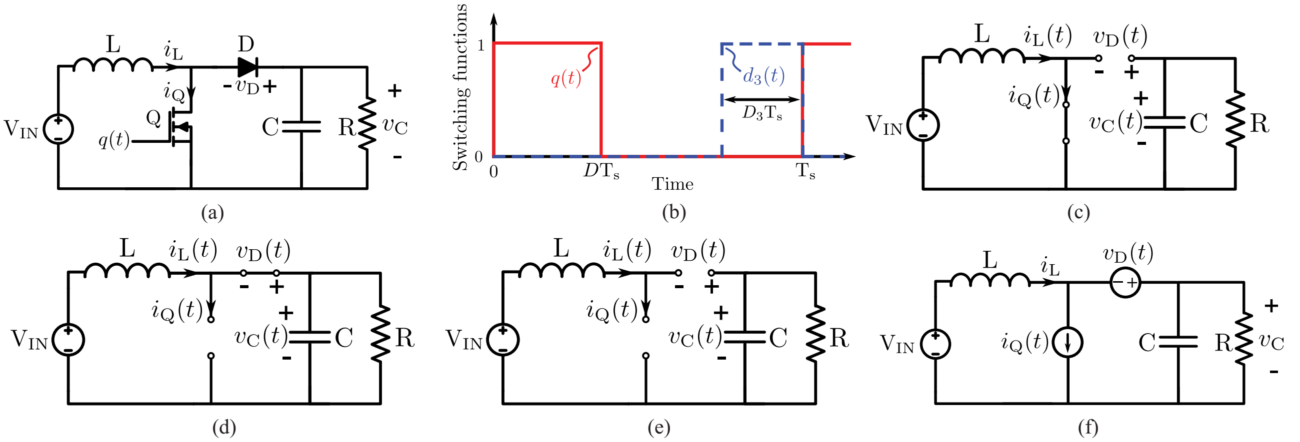

Fig. 5. Boost converter: (a) topology, (b) switching function q(t) which serves as the control signal for the active switch, along with a switching function $d_3(t)$ used to model the third subinterval under DCM operation, (c) equivalent circuit during first subinterval $q(t) = 1$ and $d_3(t) = 0$, (d) equivalent circuit during second subinterval $q(t) = 0$ and $d_3(t) = 0$, (e) equivalent circuit during third subinterval if under DCM operation $q(t) = 0$ and $d_3(t) = 1$, and (f) switched-mode equivalent circuit model.

B. Interior Switch-Network Converters

In interior switch-network converters, where switching action reconfigures the interconnection between the converter's energy storage elements, the voltage across and the current through at least some switches depends on both the energy storage elements and the actual/equivalent sources connected at the input/output ports of the converter. These interior switches (or switch networks) cannot simply be replaced by independent voltage or current sources with values determined solely from the actual/equivalent sources connected at the input/output ports. Hence, the approach presented to model edge switch-network converters will not work for this class of converters. Instead, an additional initial step (M0) must be introduced, and the remaining steps appropriately modified, to enable interior switch-network converters to be modeled in the form of an ODE, as given below.

M0) Determine analytical expressions for either the current through or the voltage across each interior switch of the converter across all subintervals under steady-state operation using the following procedure: for each subinterval of the converter, starting with the first subinterval, solve the linear circuit for that subinterval to determine analytical expressions for the currents through the switches, which are closed during the first subinterval, and for the voltages across the switches, which are open during the first subinterval, in terms of the known circuit parameters, any unknown subinterval durations, and one state variable of the converter with an unknown initial value at the start of the first subinterval.

M2) Create an equivalent circuit model for the converter by replacing the interior switches whose currents were determined in step (M0) by periodic discontinuous independent current sources with values given by the previously determined analytical expressions, and the switches whose voltages were determined in step (M0) by periodic discontinuous independent voltage sources with values given by the previously determined analytical expressions. Any noninterior switches, or switch networks, can still be replaced by independent voltage or current sources with values determined solely from the actual/equivalent sources connected at the input/output ports.

M3) Determine the converter's governing differential equation from the equivalent circuit model in terms of the state variable selected in step (M0). This will be a constant-coefficient nonhomogeneous ODE of the form of (1).

As an example, consider the boost converter shown in Fig. 5(a). Unlike the buck converter, switching action reconfigures the interconnection between its inductor and capacitor (i.e., its energy storage elements). Therefore, to model the boost converter in the form of (1) the procedure outlined for the interior switch-network converter has to be followed. Following step (M0), and assuming that the converter is operating in CCM with its active switch controlled by the switching function $q(t)$ shown in Fig. 5(b), the boost converter reduces to one of the two linear equivalent circuits shown in Fig. 5(c) and (d) in its two subintervals. Hence, the voltage across the diode D is given by $v_D(t) = q(t)v_C(t)$ and the current through the transistor Q is given by $i_Q(t) = q(t)i_L(t)$. Furthermore, the equivalent circuit of Fig. 5(c) can be solved to determine $v_C(t)$ and $i_L(t)$ for the subinterval corresponding to $q(t) = 1$

$$v_C(t) = v_C(0)e^{-\frac{t}{RC}} \tag{12}$$

$$i_L(t) = \frac{V_{IN}}{L}t + Cv'_C(0) + \frac{v_C(0)}{R} \tag{13}$$

resulting in

$$v_D(t) = q(t)\left(v_C(0)e^{-\frac{t}{RC}}\right) \tag{14}$$

$$i_Q(t) = q(t)\left(\frac{V_{IN}}{L}t + Cv'_C(0) + \frac{v_C(0)}{R}\right). \tag{15}$$

Following step (M1), the boost converter can now be modeled by the circuit shown in Fig. 5(f), where the values of the independent voltage and current source are given by (14) and (15), respectively. Finally, following step (M2), the steady-state behavior of the boost converter can be described by the following constant coefficient ODE, which is of the form of (1):

$$\mathrm{LC}\frac{d^2v_{\mathrm{C}}}{dt^2}+\frac{\mathrm{L}}{\mathrm{R}}\frac{dv_C}{dt}+v_{\mathrm{C}}(t)=\mathrm{V_{IN}}+v_{\mathrm{D}}(t)-\mathrm{L}\frac{di_{\mathrm{Q}}(t)}{dt}=f(t). \tag{16}$$

Here, the periodic and discontinuous input of the ODE $f(t)$ $(= \mathrm{V_{IN}} + v_{\mathrm{D}}(t) - \mathrm{L}\frac{di_{\mathrm{Q}}(t)}{dt})$ is given by (17) shown at the bottom of the page. In (17), $\delta(t)$ is an impulse function that appears due to the differentiation of the discontinuous function $q(t)$. Now, the procedure given in Section II-B can be used to find the steady-state solution of (16). Following step (S1), $F(s)$ (the Laplace transform of $f(t)$) is obtained from (17). Following step (S2), the roots of the characteristic polynomial associated with (16) are given by

$$s_{1,2}=\frac{1}{2\mathrm{RC}}\left(-1\pm\sqrt{1-4\frac{\mathrm{R^2C}}{\mathrm{L}}}\right)\equiv s_r\pm s_m. \tag{18}$$

Next, following step (S3), and formulating $Q(s_k) = F(s_k)$ for $k = 1, 2$ in the form of (5) and solving it for the initial conditions gives the following steady-state initial conditions:

$$\begin{aligned} v_{\mathrm{C}}(0) &= \frac{B(s_1)C(s_2)-C(s_1)B(s_2)}{A(s_2)B(s_1)-B(s_2)A(s_1)}, v'_{\mathrm{C}}(0)\\ &= \frac{C(s_1)A(s_2)-A(s_1)C(s_2)}{A(s_2)B(s_1)-B(s_2)A(s_1)} \end{aligned} \tag{19}$$

where $A(s) = \frac{\mathrm{L}}{\mathrm{R}}(1-e^{-sD\mathrm{T_s}}) + \frac{1-e^{-s\mathrm{T_s}}}{s} - \frac{1-e^{-(s+\frac{1}{\mathrm{RC}})D\mathrm{T_s}}}{s+\frac{1}{\mathrm{RC}}}$, $B(s) = \mathrm{LC}(e^{-s\mathrm{T_s}} - e^{-sD\mathrm{T_s}})$, and $C(s) = \frac{\mathrm{V_{IN}}}{s}(e^{-sD\mathrm{T_s}} - e^{-s\mathrm{T_s}}) + \mathrm{V_{IN}}D\mathrm{T_s}e^{-sD\mathrm{T_s}}$. Finally, following step (S4), and solving (16) across one switching period using the obtained initial conditions, yields the following output voltage, (20) shown at bottom of this page, where $k_1 = (v_{\mathrm{C}}(0)e^{-D\mathrm{T_s}/\mathrm{RC}} - \mathrm{V_{IN}})$ and $k_2 = \frac{\mathrm{V_{IN}}D\mathrm{T_s}}{\mathrm{LC}} + \frac{v_{\mathrm{C}}(0)}{\mathrm{RC}} + v'_{\mathrm{C}}(0) + s_r(\mathrm{V_{IN}} + v_{\mathrm{C}}(0)e^{-D\mathrm{T_s}/\mathrm{RC}})$.

As expected $v_{\mathrm{C}}(t)$ has a first order response for $0 \le t < D\mathrm{T_s}$ as the inductor and capacitor are disconnected during the first subinterval. To validate the accuracy of the closed-form expression for the output voltage waveform given by (20), it is compared with a simulated steady-state waveform generated using PSIM in Fig. 6 for an example boost converter design. The LBSM and PSIM results are identical. Fig. 6 also plots the output voltage waveform of the boost converter obtained using small ripple approximation. The output voltage waveform, and the associated voltage ripple, predicted by small ripple approximation is quite different from the actual one predicted by numerical simulation and LBSM. Hence, the waveform obtained using LBSM can be used to analyze and design the boost converter more accurately than small ripple approximation. The values of normalized average output voltage (i.e., voltage gain) as predicted by LBSM and small ripple approximation are compared for a range of duty cycle in Fig. 7. It is interesting to note that small ripple approximation overestimates the voltage gain. Furthermore, small ripple approximation does not

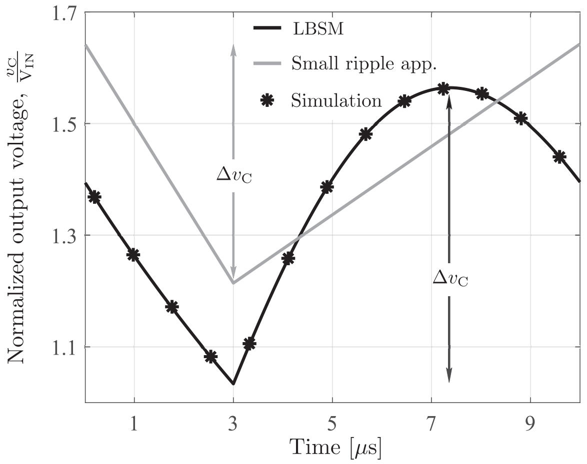

Fig. 6. Comparison of normalized output voltage waveform obtained using LBSM, numerical simulation, and small ripple approximation for a boost converter with the following parameter values: $\mathrm{L} = 1\,\mu\mathrm{H}$, $\mathrm{C} = 10\,\mu\mathrm{F}$, $\mathrm{R} = 1\,\Omega$, $D = 0.3$, and $f_s = 100\,\mathrm{kHz}$. Here, $\Delta v_{\mathrm{C}}/\mathrm{V_C}$ is 39% and 30% for the LBSM and small ripple approximation waveforms, respectively.

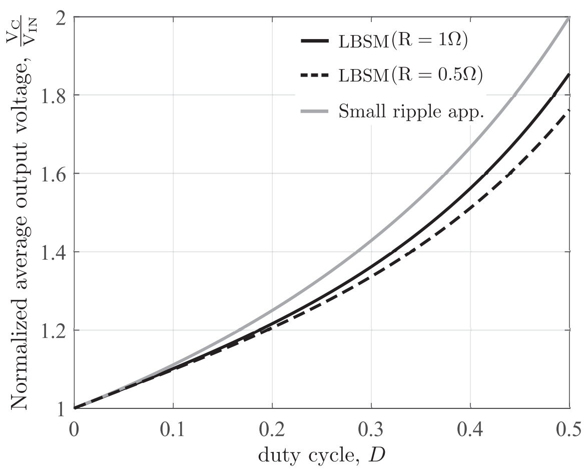

Fig. 7. Comparison of normalized average output voltage $\mathrm{V_C}/\mathrm{V_{IN}}$ (i.e., voltage gain) as function of duty cycle obtained using LBSM and small ripple approximation for the example boost converter of Fig. 6.

$$f(t)=\begin{cases} v_{\mathrm{C}}(0)e^{-\frac{t}{\mathrm{RC}}}-\left(\mathrm{LC}v'_{\mathrm{C}}(0)+\frac{\mathrm{L}}{\mathrm{R}}v_{\mathrm{C}}(0)\right)\delta(t) & 0\le t<D\mathrm{T_s}\\ \mathrm{V_{IN}}+\left(\mathrm{LC}v'_{\mathrm{C}}(0)+\frac{\mathrm{L}}{\mathrm{R}}v_{\mathrm{C}}(0)+\mathrm{V_{IN}}D\mathrm{T_s}\right)\delta(t-D\mathrm{T_s}) & D\mathrm{T_s}\le t<\mathrm{T_s} \end{cases} \tag{17}$$

$$v_{\mathrm{C}}(t)=\begin{cases} v_{\mathrm{C}}(0)e^{-\frac{t}{\mathrm{RC}}} & 0\le t<D\mathrm{T_s}\\ \mathrm{V_{IN}}+e^{s_r(t-D\mathrm{T_s})}\left[k_1\cosh\left(s_m(t-D\mathrm{T_s})\right)+\dfrac{k_2}{s_m}\sinh\left(s_m(t-D\mathrm{T_s})\right)\right] & D\mathrm{T_s}\le t<\mathrm{T}_s \end{cases} \tag{20}$$

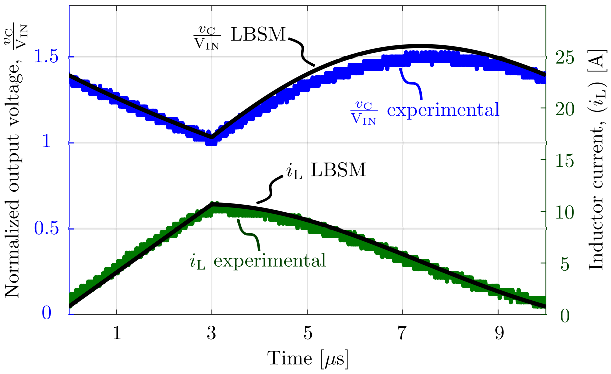

Fig. 8. Comparison of normalized output voltage (v_C/V_{IN}) and inductor current (i_L) waveforms obtained using LBSM and experimental measurement for a boost converter operating in CCM with following parameter values: $V_{IN} = 3.3$ V, $L = 1$ μH, $C = 10$ μF, $R = 1$ Ω, $D = 0.3$, and $f_s = 100$ kHz.

predict the dependence of voltage gain on load resistance. In reality, the voltage gain decreases with increased loading and this decrease is more pronounced at larger duty cycles, as can be seen from Fig. 7. Small ripple approximation overestimates the voltage gain for a boost converter because it uses the average value of the output voltage across the full switching period V_{OUT} as the average value of the output voltage during the second subinterval ($DT_s < t < T_s$) while applying volt-second balance for inductor L. Hence, it incorrectly predicts the average output voltage of the converter to be V_{IN}/D', while in reality this is the average value of the output voltage during the second subinterval. Since, V_{OUT} is less than the average value of the output voltage in the second subinterval (see LBSM predicted output voltage waveform of Fig. 6), the average output voltage is less than V_{IN}/D'. To experimentally validate the waveforms predicted by LBSM for the boost converter operating in CCM, a boost converter is built using the Texas Instruments LMG5200EVM-02 GaN power stage evaluation board. The parameter values for this prototyped boost converter are: $V_{IN} = 3.3$ V, $L = 1$ μH, $C = 10$ μF, $R = 1$ Ω, $D = 0.3$, and $f_s = 100$ kHz. The experimentally measured output voltage and inductor current waveforms for the boost converter operating in CCM are compared with the LBSM predicted waveforms in Fig. 8. There is a good match in the shape of the LBSM and the experimental waveforms. The slight discrepancy between these waveforms is due to the losses in the experimental prototype, which have not been accounted for in the theoretical analysis.

LBSM can also model the boost converter under DCM operation. Under this operating mode, the boost converter of Fig. 5(a) has three subintervals, the first two of which are identical to the subintervals under CCM operation. To model the third subinterval, a new switching function $d_3(t)$ is introduced, as shown in Fig. 5(b). The duration of this third subinterval (D_3T_s) is not known *a priori*, and will have to be determined by LBSM. Again following the modeling procedure for interior switch-network converters, starting with step (M0), the boost converter under DCM operation reduces to one of the three linear equivalent circuits shown in Fig. 5(c)–(e) in its three subintervals. Hence, the voltage across the diode D is given by $v_D(t) = q(t)v_C(t) + d_3(t)(v_C(t) - V_{IN})$ and the current through the transistor Q is given by $i_Q(t) = q(t)i_L(t)$. Furthermore, the equivalent circuits of Fig. 5(c) and (e) can be solved to determine $v_C(t)$ and $i_L(t)$ during the first ($q(t) = 1$ and $d_3(t) = 0$) and the third ($q(t) = 0$ and $d_3(t) = 1$) subintervals

$$v_C(t) = \begin{cases} v_C(0)e^{-\frac{t}{RC}} & \text{if } q(t) = 1 \text{ and } d_3(t) = 0 \\ v_C(0)e^{-\frac{t-T_s}{RC}} & \text{if } q(t) = 0 \text{ and } d_3(t) = 1 \end{cases} \tag{21}$$

$$i_L(t) = \begin{cases} \frac{V_{IN}}{L}t & \text{if } q(t) = 1 \text{ and } d_3(t) = 0 \\ 0 & \text{if } q(t) = 0 \text{ and } d_3(t) = 1 \end{cases} \tag{22}$$

resulting in

$$v_D(t) = q(t)\left(v_C(0)e^{-\frac{t}{RC}}\right) + d_3(t)\left(v_C(0)e^{-\frac{t-T_s}{RC}} - V_{IN}\right) \tag{23}$$

$$i_Q(t) = q(t)\frac{V_{IN}}{L}t. \tag{24}$$

Following step (M1), the boost converter in DCM can also be modeled by the circuit shown in Fig. 5(f), but with the values of the independent voltage and current source given by (23) and (24), respectively. Finally, following step (M2), the steady-state behavior of the boost converter is again described by (16), however, with input $f(t)$ $(= V_{IN} + v_D(t) - L\frac{di_Q(t)}{dt})$ given by

$$f(t) = \begin{cases} v_C(0)e^{-\frac{t}{RC}} & 0 \le t < DT_s \\ V_{IN} + V_{IN}DT_s\delta(t - DT_s) & DT_s \le t < (1 - D_3)T_s \\ v_C(0)e^{-\frac{t-T_s}{RC}} & (1 - D_3)T_s \le t < T_s. \end{cases} \tag{25}$$

In the first step (S1) towards finding the steady-state solution of the ODE modeling the boost converter in DCM, $F(s)$ is obtained from (25). In the second step (S2), the roots of the characteristic polynomial come out to be the same as those for the boost converter in CCM as given by (18). In step (S3), by formulating $Q(s_k) = F(s_k)$ for $k = 1, 2$ and solving it for the initial conditions gives

$$v_C(0) = \frac{B(s_1)C(s_2) - C(s_1)B(s_2)}{A(s_2)B(s_1) - B(s_2)A(s_1)}, v_C'(0) = \frac{C(s_1)A(s_2) - A(s_1)C(s_2)}{A(s_2)B(s_1) - B(s_2)A(s_1)} \tag{26}$$

where: $A(s) = \frac{1-e^{-sT_s}}{s} - (e^{(s+\frac{1}{RC})(1-D_3)T_s})/(s + \frac{1}{RC})$, $B(s) = LC(e^{-sT_s} - 1)$, and $C(s) = \frac{V_{IN}}{s}(e^{-sDT_s} - e^{-s(1-D_3T_s)}) + V_{IN}DT_se^{-sDT_s}$. Note that both $v_C(0)$ and $v_C'(0)$ are in terms of D_3, which is unknown. However, under DCM operation, the steady state initial conditions $v_C(0)$ and $v_C'(0)$ are not independent of each other and are related by

$$Cv_C'(0) = -v_C(0)/R \tag{27}$$

as in the third subinterval the capacitor current is equal to the negative of the load current, and the end of the third subinterval coincides with the start of the first subinterval (i.e., this current relationship holds at $t = 0$). Substituting (26) into (27), yields

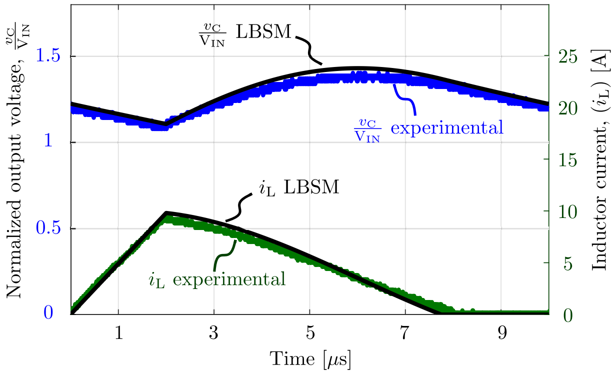

Fig. 9. Comparison of normalized output voltage (v_C/V_{IN}) and inductor current (i_L) waveforms obtained using LBSM and experimental measurement for a boost converter operating in DCM with following parameter values: $V_{IN} = 5$ V, $L = 1$ μH, $C = 10$ μF, $R = 2$ Ω, $D = 0.2$, and $f_s = 100$ kHz.

the following equation for D_3:

$$\begin{aligned} &-u_1(s_1)\, e^{s_1(1-D_3)} \quad +u_1(s_2)\, e^{s_2(1-D_3)} \\ &-u_2(s_1)\, e^{-s_1(1-D_3)} \quad +u_2(s_2)\, e^{-s_2(1-D_3)} = u_3(s_1, s_2) \end{aligned} \tag{28}$$

where u_1, u_2, and u_3 are given at the bottom of this page. As (28) is a transcendental equation it does not have a closed form solution; however, it can be solved numerically for D_3. Once D_3 is computed, it can be substituted into (26) to determine the steady-state initial conditions for the boost converter in DCM. Finally, following step (S4), and solving (16) across one switching period using the obtained initial conditions, yields the output voltage as shown by (29) at the bottom of this page, where $k_1 = (v_C(0)e^{-DT_s/RC} - V_{IN})$, $k_2 = \frac{V_{IN}DT_s}{LC} + s_r(V_{IN} + v_C(0)e^{-DT_s/RC})$, and $D_3' = 1 - D_3$. The inductor current under DCM operation can also be obtained using (22) in first and third subintervals and (29) shown at the bottom of the page, in the second subinterval. The LBSM predicted output voltage and inductor current waveforms for a boost converter operating under DCM are compared with experimental results in Fig. 9, which shows a good match between the LBSM predicted and experimental waveforms.

In addition to dc–dc converters, LBSM can also be used to accurately predict the waveforms of dc–ac and ac–dc converters. This is because LBSM can predict waveform dynamics within a switching period irrespective of whether the external (output or input) voltages are constant (as in dc–dc converters) or time varying (as in dc–ac and ac–dc converters). When the external voltages are time varying, the periodicity used in LBSM must be selected so as to capture the periodicity of its steady-state waveforms. In the case when the output (or input) ac voltage of the dc–ac (or ac–dc) converter has the same periodicity as the converter's switching period (such as in resonant inverters and line-commutated rectifiers), then the steady-state waveforms of the converter will be periodic with a period equal to its switching period; and in this case, the periodicity used in LBSM is simply the switching period. On the other hand, if the output (or input) ac voltage of the dc–ac (or ac–dc) converter varies more slowly than its switching period (such as in line-interfaced high-frequency inverters and power factor correction rectifiers), then, assuming an integer relationship between the switching and the external ac frequency, the steady-state waveforms of the converter will be periodic with a period equal to the period of the external ac voltage; and in this case, the periodicity used in LBSM is the period of the external ac voltage. In this later case, LBSM will involve a relatively large number of subintervals, and the state-space formulation of LBSM (as given in Appendix II) will be easier to utilize. The application of LBSM to an example of each type of dc–ac converter is demonstrated in Appendix III.

IV. ANALYSIS AND DESIGN OF SERIES RESONANT CONVERTER AND PHASE-SHIFT CONVERTER USING LBSM

In addition to hard-switching PWM converters, the LBSM technique can also be leveraged for the analysis and design of isolated soft-switching converters. Because of its accuracy LBSM captures the intracycle dynamics of such converters, which allows a detailed study of their soft-switching range and performance. Two isolated soft-switching converters, the

$$u_1(s) = \frac{2e^{\left(-T_s\left(sD-\left(s+\frac{1}{RC}\right)\right)\right)}(sDT_s+1)}{s(e^{sT_s}-1)(e^{-sT_s}-1)},\; u_2(s) = \left(2LC\left(s+\frac{1}{RC}\right)+\frac{2\left(e^{\left(s+\frac{1}{RC}\right)T_s}+e^{sDT_s}-1\right)}{s\left(e^{\left(s+\frac{1}{RC}\right)T_s}-1\right)}\right)\Big/\left(s\left(e^{-sT_s}-1\right)\right),\; u_3(s_1,s_2) =$$

$$\begin{aligned} &-\left(LC(s_1-s_2)+\frac{e^{-s_2T_s}+e^{s_1DT_s}-1}{s_1\left(e^{-s_1T_s}-1\right)}-\frac{e^{-s_1T_s}+e^{s_2DT_s}-1}{s_2\left(e^{-s_2T_s}-1\right)}\right)\left(\frac{DT_se^{-s_1DT_s}}{e^{-s_1T_s}-1}+\frac{DT_se^{-s_2DT_s}}{e^{-s_2T_s}-1}+\frac{e^{-s_1DT_s}}{s_1\left(e^{-s_1T_s}-1\right)}+\frac{e^{-s_2DT_s}}{s_2\left(e^{-s_2T_s}-1\right)}\right) \\ &+\left(LC(s_1+s_2)-\frac{e^{-s_2T_s}+e^{s_1DT_s}-1}{s_1\left(e^{-s_1T_s}-1\right)}-\frac{e^{-s_1T_s}+e^{s_2DT_s}-1}{s_2\left(e^{-s_2T_s}-1\right)}\right)\left(\frac{DT_se^{-s_1DT_s}}{e^{-s_1T_s}-1}-\frac{DT_se^{-s_2DT_s}}{e^{-s_2T_s}-1}+\frac{e^{-s_1DT_s}}{s_1\left(e^{-s_1T_s}-1\right)}-\frac{e^{-s_2DT_s}}{s_2\left(e^{-s_2T_s}-1\right)}\right) \\ &+\frac{2e^{\frac{T_s}{RC}}}{(s_2)^2\left(e^{-s_2T_s}-1\right)\left(e^{-s_1T_s}-1\right)}-\frac{2e^{\frac{T_s}{RC}}}{(s_1)^2\left(e^{-s_2T_s}-1\right)\left(e^{-s_1T_s}-1\right)} \end{aligned}$$

$$v_C(t) = \begin{cases} v_C(0)e^{-\frac{t}{RC}} & 0 \le t < DT_s \\ V_{IN} + e^{s_r(t-DT_s)}\left[k_1\cosh\left(s_m(t-DT_s)\right) + \frac{k_2}{s_m}\sinh\left(s_m(t-DT_s)\right)\right] & DT_s \le t < D_3'T_s \\ v_C(0)e^{-\frac{t-T_s}{RC}} & D_3'T_s \le t < T_s \end{cases} \tag{29}$$

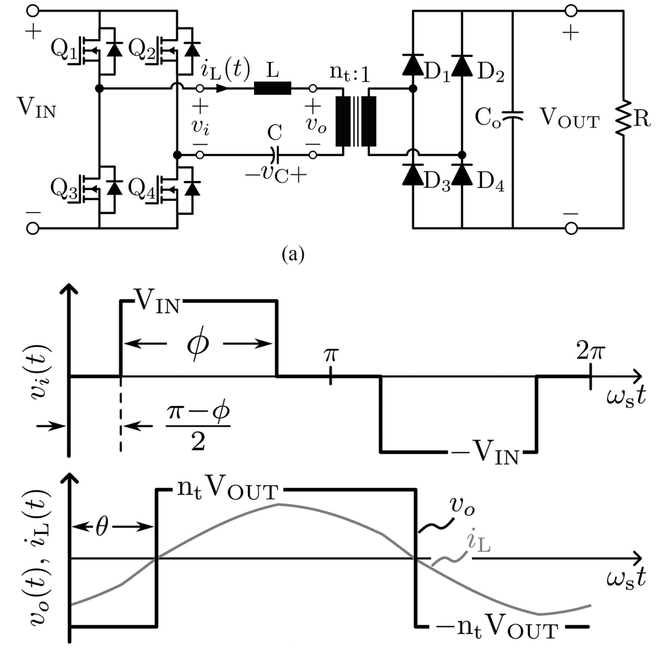

(a)

(b)

Fig. 10. SRC: (a) topology, and (b) typical waveforms under phase-shift control while maintaining ZVS.

phase-shift controlled series resonant converter (SRC) and the phase-shift converter (PSC), are investigated in this section.

A. Phase-Shift Controlled SRC

Fig. 10 shows the topology of the SRC and its typical waveforms when operating under phase-shift control while maintaining ZVS. An ODE for this converter can be derived using steps (M1) and (M2) of LBSM for edge-switch network converters

$$\mathrm{LC}\frac{d^2 v_\mathrm{C}}{dt^2} + v_\mathrm{C} = v_i(t) - v_o(t) \tag{30}$$

where $v_i(t)$ and $v_o(t)$ are as shown in Fig. 10(b). In Fig. 10(b), the waveform for $v_o(t)$ assumes a large output capacitor $\mathrm{C_o}$, so that the output voltage can be considered constant and an equivalent voltage source connected at the converter's output port can replace the load resistor. Using steps (S1)–(S4) of Section II-B, and under the condition that ZVS is maintained (i.e., $\frac{\pi-\phi}{2} < \theta$), the steady-state solution for (30) is

$$v_\mathrm{C}(t) = \begin{cases} e_1(t) + e_3(t) & 0 \le \omega_s t < \frac{\pi-\phi}{2} \\ e_2(t) + e_3(t) & \frac{\pi-\phi}{2} \le \omega_s t < \theta \\ e_2(t) + e_4(t) & \theta \le \omega_s t < \frac{\pi+\phi}{2} \\ -e_1(t - \frac{\pi}{F\omega_r}) + e_4(t) & \frac{\pi+\phi}{2} \le \omega_s t < \pi \end{cases} \tag{31}$$

where $e_1(t) = -\mathrm{V_{IN}}\frac{\sin(\frac{\phi}{2F})}{\cos(\frac{\pi}{2F})}\sin(\omega_r t)$, $e_2(t) = -\mathrm{V_{IN}}\frac{\sin(\frac{\phi}{2F})}{\cos(\frac{\pi}{2F})}\sin(\omega_r t) + \mathrm{V_{IN}}(1 - \cos(\omega_r t - \frac{\pi-\phi}{2F}))$, $e_3(t) = \mathrm{MV_{IN}}[1 + \tan(\frac{\pi}{2F})\sin(\omega_r t - \frac{\theta}{F}) - \cos(\omega_r t - \frac{\theta}{F})]$, and $e_4(t) = \mathrm{MV_{IN}}[-1 + \tan(\frac{\pi}{2F})\sin(\omega_r t - \frac{\theta}{F}) + \cos(\omega_r t - \frac{\theta}{F})]$. Here, $\mathrm{M} = \frac{\mathrm{n_t V_{OUT}}}{\mathrm{V_{IN}}}$ is converter voltage gain without the transformer, $0 \le \phi \le \pi$ is the phase shift between the two half-bridges of the inverter, $\omega_r = 1/\sqrt{\mathrm{LC}}$ is the radial resonant frequency, ω_s is the radial switching frequency and $F = \omega_s/\omega_r$ is the normalized switching frequency of the converter. An expression for the inductor current i_L can be determined from (31) as it is equal to the capacitor current. The two unknowns in (31), voltage gain M and current phase lag angle θ, can be determined by imposing capacitor charge balance and setting i_L to zero at $\omega_s t = \theta$

$$\mathrm{M} = \left(\frac{2F}{\pi Q}\right)\frac{AB\sqrt{A^2+B^2-1} - B^2}{A^2+B^2} \tag{32}$$

$$\theta = \frac{\pi}{2} - F\sin^{-1}\left(\frac{A\sqrt{A^2+B^2-1} - B}{A^2+B^2}\right) \tag{33}$$

where $A = \sin(\frac{\phi}{2F})\tan(\frac{\pi}{2F}) + \cos(\frac{\phi}{2F})$, and $B = {(\pi Q\cos(\frac{\pi-\phi}{2F}))}/{(2F\sin(\frac{\pi}{2F}))}$, $Q = {\mathrm{Z_0}}/{(\mathrm{n_t}^2\mathrm{R})}$ is the loaded quality factor, and $\mathrm{Z_0} = \sqrt{L/C}$ is the characteristic impedance. By equating θ as given by (33) to $\frac{\pi-\phi}{2F}$, the phase-shift associated with the ZVS boundary of the converter ϕ_ZVS can be obtained

$$\phi_\mathrm{ZVS} = \pi - 2F\cos^{-1}\left(\left(1 + \left(\frac{\pi Q}{2F}\cot\frac{\pi}{2F}\right)^2\right)^{-\frac{1}{2}}\right). \tag{34}$$

To evaluate the benefits of the accurate waveforms determined using LBSM, consider an example 100-W constant output power SRC with a constant output voltage $\mathrm{V_{OUT}} = 40\,\mathrm{V}$, in which variations in input voltage from $\mathrm{V_{IN,min}} = 100\,\mathrm{V}$ to $\mathrm{V_{IN,max}} = 330\,\mathrm{V}$ are compensated for using phase-shift control. Assuming the SRC is required to always operate under ZVS, and regulation is done by decreasing the phase shift from π to ϕ_ZVS, the ratio of the SRC voltage gain at π phase shift to its voltage gain at ϕ_ZVS is given by

$$\frac{\mathrm{M}\,(\phi = \pi)}{\mathrm{M}\,(\phi = \phi_\mathrm{ZVS})} = \frac{\mathrm{V_{IN,max}}}{\mathrm{V_{IN,min}}}. \tag{35}$$

Substituting (32) and (34) into (35) and simplifying gives

$$\frac{\tan(\gamma)\sqrt{\tan^2(\gamma) + (\gamma Q\csc(\gamma))^2} - \gamma Q}{\tan^2(\gamma) - \gamma Q} = \frac{\mathrm{V_{IN,max}}}{\mathrm{V_{IN,min}}} \tag{36}$$

where $\gamma = \frac{\pi}{2F}$. Equation (36) can be used to determine the appropriate loaded quality factor Q when the normalized switching frequency F is known. Typically, phase-shift control is activated when the effectiveness of frequency control diminishes [24]. Assuming that in our example phase-shift control becomes active at $F = 1.4$, the appropriate value of $Q = 2.5$. Using (32), the voltage gain of the converter when $\phi = \pi$ is $\mathrm{M} = 0.408$. As the converter has maximum voltage gain at $\phi = \pi$, it uses this phase shift when the input voltage is at its minimum. Hence, the transformer turns ratio can be computed using $\mathrm{n_t} = \frac{\mathrm{M}(\phi=\pi)\mathrm{V_{IN,min}}}{\mathrm{V_{OUT}}}$ and its value is 1.02. Assuming $F = 1.4$ corresponds to 100 kHz switching frequency, the resonant tank component values can be computed using the defining expressions for F and Q, and their values are given by $\mathrm{L} = 89\,\mu\mathrm{H}$ and $\mathrm{C} = 55\,\mathrm{nF}$. The conventional method for designing a phase-shift controlled SRC relies upon fundamental harmonic analysis (FHA), which yields the

TABLE I
SIMULATION RESULTS FOR LBSM- AND FHA-BASED DESIGNED SRC WITH CONVERTER OPERATING CONDITIONS AS: INPUT VOLTAGE ($\mathrm{V_{IN}}$) OF 100 V, OUTPUT VOLTAGE ($\mathrm{V_{OUT}}$) OF 40 V, INVERTER PHASE SHIFT ϕ OF 180°, AND OUTPUT POWER OF 100 W

Design method	F	Q	$\mathrm{M}(\phi=\pi)$	$\mathrm{I_{L,rms}}$ [A]	$0.5\mathrm{LI_{L,pk}}^2$ [μJ]	$0.5\mathrm{CV_{C,pk}}^2$ [μJ]
FHA	1.4	3.5	0.303	3.9	1247	519
LBSM	1.4	2.5	0.408	2.9	835	365

following design equation:

$$\frac{\mathrm{M}\left(\phi=\pi\right)}{\mathrm{M}\left(\phi=\phi_{\mathrm{ZVS}}\right)}=\frac{\sqrt{64/\pi^4+\left(Q(F-1/F)\right)^2}}{8/\pi^2}=\frac{\mathrm{V_{IN,max}}}{\mathrm{V_{IN,min}}} \tag{37}$$

which is analogous to LBSM's (36). For $F=1.4$, the FHA based design gives $Q=3.5$, $\mathrm{M}=0.303$, $\mathrm{n_t}=0.75$, $\mathrm{L}=70\,\mu\mathrm{H}$, and $\mathrm{C}=71\,\mathrm{nF}$. The FHA- and LBSM-based designs are compared in Table I. The inductor rms current and the peak energy stored in the inductor and the capacitor are determined through simulations for both converters. Since the LBSM-based design provides a higher voltage gain M, and a correspondingly higher transformer turns ratio, it imposes lower current and voltage stresses on the resonant tank elements compared to the FHA based design. This substantial benefit due to the higher voltage gain is not negated by the LBSM-based design's lower tank Q value and potentially increased losses due to higher order harmonics, as any higher order harmonics in the tank current also contribute to real power transfer (further lowering inductor rms current) and generally assist in achieving ZVS. In fact, the lower tank Q enables the use of a smaller inductance value inductor (hence, lower effective series resistance given an inductor quality factor), which combined with the lower rms inductor current results in substantially lower losses. In the considered example, the 26% lower inductor rms current of the LBSM-based design would result in 45% reduction in primary side conduction losses. Furthermore, the 32% lower peak stored energy in the resonant tank would enable the tank elements of the LBSM based design to be substantially smaller in size.

B. Phase-Shift Converter

Topologically, the PSC with capacitive filter is identical to the SRC except that it does not have the resonant capacitor [see Fig. 10(a)]. Mathematically, the PSC can be derived from the SRC by taking the limit $\mathrm{C}\to\infty$, which would effectively short circuit the resonant capacitor. Therefore, the expression for the current waveform of the PSC can be derived simply by making the resonant capacitor infinitely large in the expression for the current waveform of the SRC. Making the resonant capacitor $\mathrm{C}\to\infty$ results in $Q\to 0$ and $F\to\infty$. Therefore, the voltage gain and the current phase lag angle under ZVS operation, and the ZVS boundary (ϕ_{ZVS}) for the PSC can be obtained from (32)–(34) under the limit $Q\to 0$ and $F\to\infty$

$$\mathrm{M}=\frac{1}{\pi}\left(\sqrt{\phi(2\pi-\phi)+\left(2Q_{\mathrm{L}}\right)^2}-2Q_{\mathrm{L}}\right) \tag{38}$$

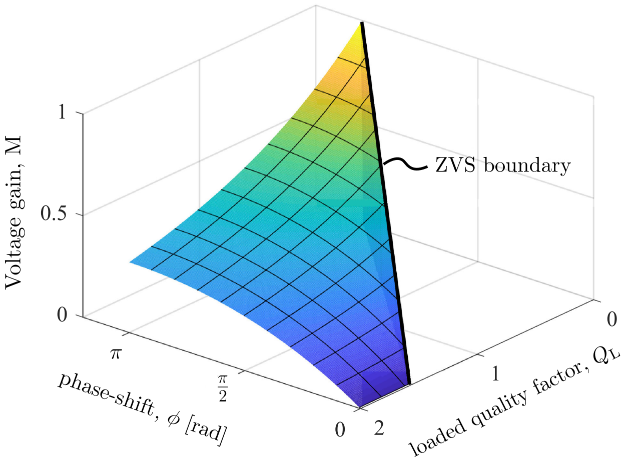

Fig. 11. Voltage gain M as a function of phase shift ϕ and loaded quality factor of the inductor Q_{L} in the ZVS region of the PSC.

$$\theta=\frac{\pi}{2}\left(1-\mathrm{M}\right) \tag{39}$$

$$\phi_{\mathrm{ZVS}}=\pi-2Q_{\mathrm{L}} \tag{40}$$

where $Q_{\mathrm{L}}=\frac{\omega_s\mathrm{L}}{\mathrm{n_t}^2\mathrm{R}}$ is the loaded quality factor of the inductor. At the ZVS boundary, i.e., $\phi=\phi_{\mathrm{ZVS}}$, the expression for M simplifies to

$$\mathrm{M}=1-\frac{2}{\pi}Q_{\mathrm{L}}=\frac{\phi_{\mathrm{ZVS}}}{\pi}. \tag{41}$$

A plot of voltage gain M as a function of phase shift ϕ and the loaded quality factor of the inductor Q_{L}, as given by (38), for the ZVS region of the PSC is shown in Fig. 11.

To compare the PSC with the SRC, the PSC is also designed for the same example specifications, i.e., $\mathrm{V_{IN,min}}=100\,\mathrm{V}$, $\mathrm{V_{IN,max}}=330\,\mathrm{V}$, $\mathrm{V_{OUT}}=40\,\mathrm{V}$, $P=100\,\mathrm{W}$, and $f_s=100\,\mathrm{kHz}$. Assuming the PSC is also required to operate under ZVS, and regulation is also done by decreasing the phase shift from π to ϕ_{ZVS}, the ratio of the PSC voltage gain at π phase shift to its voltage gain at ϕ_{ZVS} is given by

$$\frac{\mathrm{M}\left(\phi=\pi\right)}{\mathrm{M}\left(\phi=\phi_{\mathrm{ZVS}}\right)}=\frac{\sqrt{1+\left(\frac{2}{\pi}Q_{\mathrm{L}}\right)^2}-\frac{2}{\pi}Q_{\mathrm{L}}}{1-\frac{2}{\pi}Q_{\mathrm{L}}}=\frac{\mathrm{V_{IN,max}}}{\mathrm{V_{IN,min}}} \tag{42}$$

which is analogous to the SRC's (36). For the given specifications, (42) gives the required loaded inductor quality factor $Q_{\mathrm{L}}=1.35$. From (38), at $\phi=\pi$, the voltage gain of the converter M is 0.46. Similar to the SRC, the PSC has maximum voltage gain at $\phi=\pi$, which it uses at minimum input voltage. Hence, its transformer turns ratio $\mathrm{n_t}=\frac{\mathrm{M}(\phi=\pi)\mathrm{V_{IN,min}}}{\mathrm{V_{OUT}}}=1.15$. Given the PSC is also operating at 100 kHz switching frequency, its inductor value can be computed using the defining expression for Q_{L}, and is $\mathrm{L}=45.5\,\mu\mathrm{H}$. The key parameter and component values for the PSC are compared with those for the SRC, designed for the same example specifications, in Table II. As can be seen from Table II, for this example with an input voltage range of 3.3 to 1, the PSC provides a larger voltage gain relative to the SRC at a given phase shift and, therefore, gets to use a higher

TABLE II
PARAMETER AND COMPONENT VALUES FOR THE SRC AND THE PSC IN THE CONSIDERED EXAMPLE

Converter	Tank parameters	$\mathrm{M}(\phi=\pi)$	$\mathrm{n_t}$	Tank components
SRC	$F=1.4$, $Q=2.5$	0.408	1.02	$\mathrm{L}=89.1\,\mu$H, $\mathrm{C}=55.7\,$nF
PSC	$Q_\mathrm{L}=1.35$	0.46	1.15	$\mathrm{L}=45.5\,\mu$H

value of $\mathrm{n_t}$. Since both converters have the same fixed output current, the PSC with its higher $\mathrm{n_t}$ has a lower primary-side current irrespective of phase shift. With near-identical inverter switching losses due to ZVS and identical transformer core and secondary-side losses in both converters, the PSC with the lower primary-side currents is expected to be more efficient due to lower primary-side conduction losses and lower inductor core losses. The PSC is also expected to be smaller as it has fewer and smaller tank components.

The comparison between the PSC and the SRC can also be generalized for an arbitrary input voltage range of α to 1, where $\alpha \equiv \mathrm{V_{IN,max}}/\mathrm{V_{IN,min}}$ is the maximum-to-minimum input voltage ratio. For the PSC, using (42), Q_L can be expressed in terms of α as

$$\frac{2}{\pi}Q_\mathrm{L} = \frac{\alpha(\alpha-1)-\sqrt{2\alpha(\alpha-1)}}{\alpha(\alpha-2)}. \tag{43}$$

Substituting this expression for Q_L and $\phi=\pi$ into (38) gives an expression for the maximum voltage gain of the PSC in terms of α:

$$\mathrm{M_{PSC}}(\phi=\pi) = \frac{-\alpha+\sqrt{2\alpha(\alpha-1)}}{\alpha-2}. \tag{44}$$

For the SRC, using (32), (36) and $\phi=\pi$, an analogous expression for the maximum voltage gain is obtained in terms of α, (45) shown at bottom of this page.

Since the SRC and the PSC are operating under ZVS and have identical output currents, any difference in their efficiency will arise from differences in their primary-side currents. Hence, the most important characteristic of their designs is maximum voltage gain $\mathrm{M}(\phi=\pi)$, which determines the primary-side currents and consequently conduction losses and tank sizes. The maximum voltage gain for the PSC depends solely on α, while for the SRC it depends on both α and the normalized switching frequency F, as can be seen from (44) and (45), respectively. A plot of maximum voltage gain $\mathrm{M}(\phi=\pi)$ for the SRC and the PSC, as a function of F, for two different values of α (1.3 and 3.3) is shown in Fig. 12. As can be seen from Fig. 12, either the SRC or the PSC has the higher maximum voltage gain independent of F and depending solely on the value of α. If α is small (e.g., $\alpha=1.3$), the SRC has a larger voltage gain and is the superior design. However, if α is large (e.g., $\alpha=3.3$), the PSC provides a larger voltage gain and is superior. Another aspect to note from Fig. 12 is that the maximum voltage gain of the SRC is a monotonic function of F and as $F\to\infty$ the SRC essentially becomes the PSC. Therefore, a convenient way to determine, which converter is superior is to evaluate the maximum voltage gain of the SRC at $F\to 1$ (pure resonance) and at $F\to\infty$ (PSC). If the SRC's maximum voltage gain at $F\to 1$ is larger than its maximum voltage gain at $F\to\infty$, then the SRC is superior, otherwise the PSC is superior. The maximum voltage gain of the SRC under these two limiting values of F is

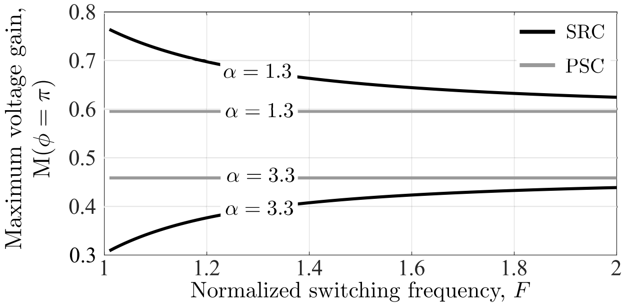

Fig. 12. Maximum voltage gain for the SRC and the PSC as a function of normalized switching frequency for maximum-to-minimum input voltage ratio $\alpha=1.3$ and $\alpha=3.3$.

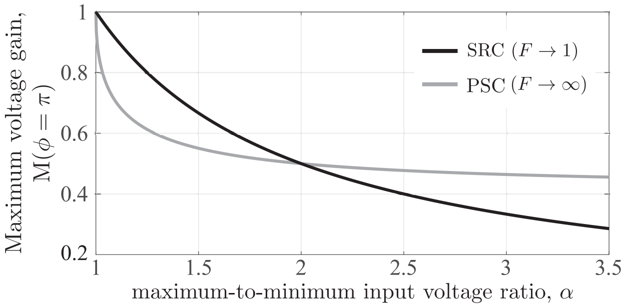

Fig. 13. Maximum voltage gain for the SRC ($F\to 1$) and the PSC ($F\to\infty$) as a function of maximum-to-minimum input voltage ratio.

$$\lim_{F\to 1}\mathrm{M_{SRC}}(\phi=\pi) = 1/\alpha \tag{46}$$

$$\lim_{F\to\infty}\mathrm{M_{SRC}}(\phi=\pi) = \frac{-\alpha+\sqrt{2\alpha(\alpha-1)}}{\alpha-2}. \tag{47}$$

The maximum voltage gains of the SRC under the two limiting values of F, as given by (46) and (47), are plotted in Fig. 13 as functions of α. As can be seen from Fig. 13, the two gains are equal when $\alpha=2$. If the maximum-to-minimum input voltage ratio $\alpha<2$, then the SRC provides the higher maximum voltage gain and is superior, and if $\alpha>2$ then the PSC provides the higher maximum voltage gain and is superior.

$$\mathrm{M_{SRC}}(\phi=\pi) = \frac{\alpha\left(\tan^2(\gamma)+(2-\alpha)\right)-(2-\alpha)\sqrt{(\alpha-1)\left(2\alpha+\tan^2(\gamma)(1+\alpha)\right)}}{\alpha^2\tan^2(\gamma)+(2-\alpha)^2} \tag{45}$$

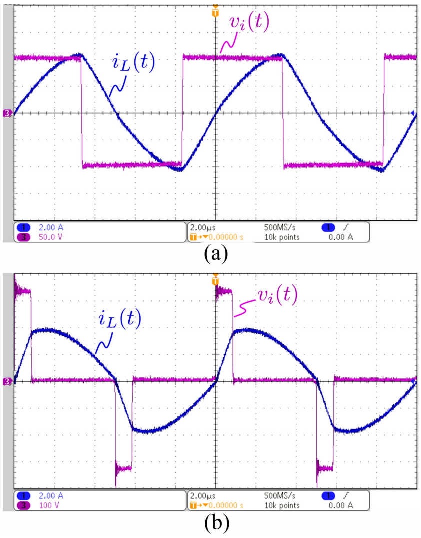

(a)
(b)

Fig. 14. Inverter output voltage $v_i(t)$ and inductor current $i_{\mathrm{L}}(t)$ of the prototyped SRC operating with (a) input voltage $\mathrm{V_{IN}} = 100\,\mathrm{V}$ and (b) input voltage $\mathrm{V_{IN}} = 330\,\mathrm{V}$.

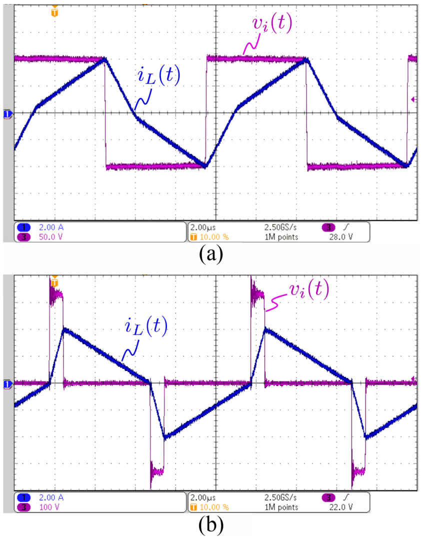

(a)
(b)

Fig. 15. Inverter output voltage $v_i(t)$ and inductor current $i_{\mathrm{L}}(t)$ of the prototyped PSC operating with (a) input voltage $\mathrm{V_{IN}} = 100\,\mathrm{V}$ and (b) input voltage $\mathrm{V_{IN}} = 330\,\mathrm{V}$.

TABLE III
COMPONENTS USED IN THE PROTOTYPED SRC AND PSC

Components	SRC	PSC
$\mathrm{Q_1}$, $\mathrm{Q_2}$, $\mathrm{Q_3}$, and $\mathrm{Q_4}$	FCB070N65S3 650-V/44-A MOSFET	FCB070N65S3 650-V/44-A MOSFET
$\mathrm{D_1}$, $\mathrm{D_2}$, $\mathrm{D_3}$, and $\mathrm{D_4}$	V3P6L 60-V/3-A Schottky diode	V3P6L 60-V/3-A Schottky diode
C	55.7-nF 630-V polypropylene film cap.	N/A
L	89.1 μH 32 turns of 140-strand AWG-38 Litz wire ETD 34/17/11 TDK N87 1.36-mm airgap	45.5 μH 32 turns of 140-strand AWG-38 Litz wire ETD 34/17/11 TDK N87 2.7-mm airgap
Transformer	1.02:1 turns ratio primary: 13 turns of 100-strand AWG-38 secondary: 13 turns of 100-strand AWG-38 E 32/16/9 TDK N87	1.15:1 turns ratio primary: 15 turns of 100-strand AWG-38 secondary: 13 turns of 100-strand AWG-38 E 32/16/9 TDK N87

V. EXPERIMENTAL VERIFICATION OF SRC AND PSC

To validate the accuracy of the LBSM-based designs, and to compare the performance of the SRC and the PSC, the two converter designs given in Table II are built and tested. The details of the hardware are shown in Table III. The converter is controlled using a Texas Instruments TMS320F28335 DSP microcontroller, which generates the gating signals for each half-bridge with a dead time of 0.4 μs and all experimental results are reported for an output power of 100 W. The experimentally measured operating waveforms for the SRC and the PSC are shown in Figs. 14 and 15, respectively, for two different values of input voltage (100 and 330 V). From Figs. 14(b) and 15(b), it can be seen that the inductor current in both converters is zero at the instant when the leading leg switches, and both converters operate on the ZVS boundary, when the input voltage is 330 V. This validates the accuracy of the LBSM-based design equations as far as predicting ZVS boundary is concerned, since both converters were designed using (35) and (42) to have a ZVS boundary at an input voltage of 330 V.

The voltage gain M of the SRC and the PSC (discounting for their transformers' turns ratios) is also experimentally measured and compared with theoretically predicted values of M across a range of switching frequencies and for two different values of phase shift, as shown in Fig. 16(a). Here, the theoretically computed values of M are calculated using (32) and (38) for the SRC and the PSC, respectively. As can be seen from Fig. 16(a), there is an excellent match between experiment and theory, validating the accuracy of the LBSM-based equations for voltage gain.

The prototyped SRC and PSC are also operated under phase-shift control while operating at a fixed switching frequency. Fig. 16(b) shows the experimentally measured voltage gain M of the two converters as a function of phase shift while operating at 100 kHz. As expected the PSC provides a larger voltage gain than the SRC across the entire range of phase shift. The theoretically calculated values of M for the SRC and the PSC, computed using (32) and (38), respectively, are also shown using the dotted lines in Fig. 16(b). As can be seen, there is an excellent match between the experimentally measured and the theoretically predicted values of M for large values of phase shift. For phase shifts below about 0.4π for SRC and 0.44π for PSC there is a small deviation between the theoretically calculated and the experimentally measured voltage gains. This deviation at low phase-shifts arises from decreased volt-seconds applied by the inverter during the dead time. The presence of dead time and non-negligible output capacitance of the inverter transistors, that were ignored in the theoretical analysis, results in a reduction of volt-seconds applied by the inverter due to the

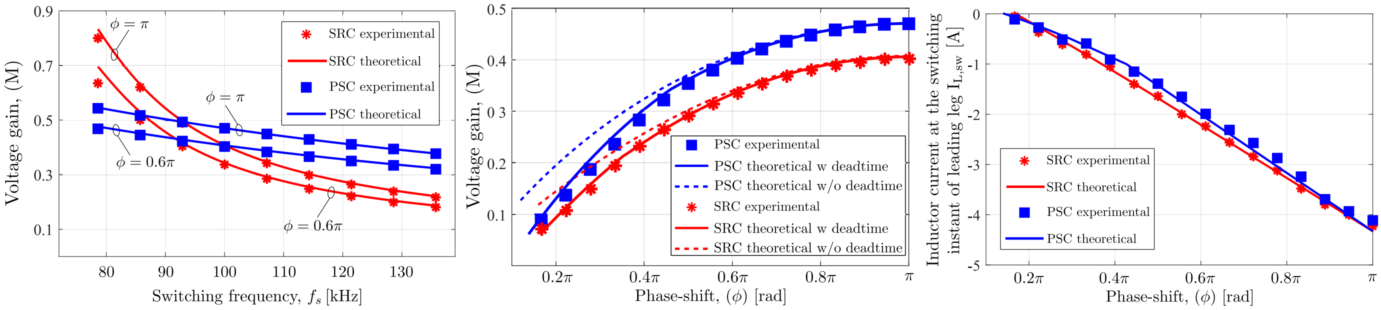

(a) (b) (c)

Fig. 16. Theoretically calculated (using LBSM) and experimentally measured for the SRC and the PSC: (a) voltage gain as a function of switching frequency for two different values of inverter phase shift, (b) voltage gain as a function of phase shift when operating at 100 kHz switching frequency, and (c) inductor current at the instant when leading leg switches ($I_{L,sw}$) as a function of inverter phase shift when operating at 100 kHz.

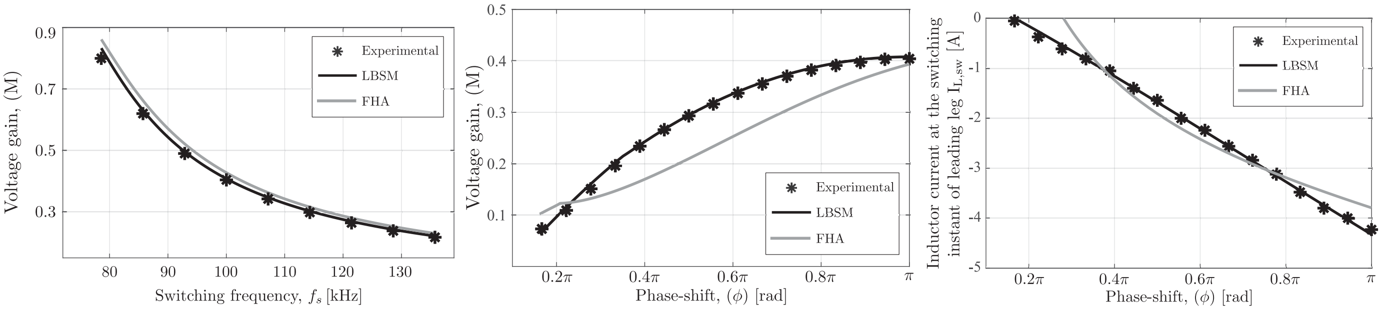

(a) (b) (c)

Fig. 17. Theoretically calculated using LBSM and FHA and experimentally measured for the SRC: (a) voltage gain as a function of switching frequency with an inverter phase shift of 180°, (b) voltage gain as a function of inverter phase shift when operating at 100 kHz switching frequency, and (c) inductor current at the instant when leading leg switches ($I_{L,sw}$) as a function of inverter phase shift when operating at 100 kHz.

extra time needed to charge/discharge these capacitances. This change in applied volt seconds can be expressed in terms of an effective phase shift ϕ_{eff}, which can then be used to determine the converter waveforms, including the inductor current and voltage gain using the already developed expressions for these in terms of phase shift ϕ based on an edge switch network model for the converter in which the dead times were not included. Following this approach, the effective phase shift ϕ_{eff} is given by:

$$\phi_{\text{eff}} = \phi - \omega_{\text{s}} \left(\Delta t - \frac{\text{Z}_{\text{oss}} \text{I}_{\text{L,sw}}}{\omega_{\text{oss}} \text{V}_{\text{IN}}} \left(1 - \cos\left(\omega_{\text{oss}} \Delta t\right)\right) \right) \quad (48)$$

where ω_{s} is the converter's radial switching frequency, $\omega_{\text{oss}}(\equiv \frac{1}{\sqrt{2\text{LC}_{\text{oss}}}})$ and $\text{Z}_{\text{oss}}(\equiv \sqrt{\frac{\text{L}}{2\text{C}_{\text{oss}}}})$ are the resonant frequency and the characteristic impedance of the tank formed by L and 2C_{oss}, respectively, $\text{I}_{\text{L,sw}}$ is the inductor current at the instant when the leading half-bridge switches (i.e., at $\omega_{\text{s}} t = \frac{\pi - \phi}{2}$), and Δt is the time taken by the inverter output voltage v_i to go from 0 V to the converter input voltage V_{IN}

$$\Delta t = \begin{cases} \frac{1}{\omega_{\text{oss}}} \sin^{-1}\left(\frac{\text{V}_{\text{IN}}}{\text{Z}_{\text{oss}} \text{I}_{\text{L,sw}}}\right) & \text{if } \text{Z}_{\text{oss}} \text{I}_{\text{L,sw}} \geq \text{V}_{\text{IN}} \\ t_{\text{d}} & \text{if } \text{Z}_{\text{oss}} \text{I}_{\text{L,sw}} < \text{V}_{\text{IN}} \end{cases} \quad (49)$$

where t_{d} is the dead time of the leading half-bridge. A derivation of (48) and (49) is given in Appendix IV. The theoretically calculated voltage gain with the dead time effect included by means of ϕ_{eff} is plotted as solid lines and compared with experimental data and the theoretical calculation without the dead time effect included in Fig. 16(b). As can be seen, there is an excellent match between theory and experiment when the dead time is included.

The theoretical calculation of voltage gain utilizing (48) and (49) relies on $\text{I}_{\text{L,sw}}$. An accurate value of $\text{I}_{\text{L,sw}}$ can be determined from the LBSM derived waveforms. Fig. 16(c) shows the theoretically calculated values of $\text{I}_{\text{L,sw}}$ for the SRC and the PSC as a function of phase shift when operating at 100 kHz switching frequency. The experimentally measured values of $\text{I}_{\text{L,sw}}$ are also shown in Fig. 16(c), and match the LBSM predicted values very well. Since the SRC can also be modeled using FHA, it is instructive to compare the predictions of the LBSM and the FHA-based models for the SRC with experimental results. This comparison is shown in Fig. 17. Clearly, the LBSM-based model provides a closer match to experiments. A comparison of LBSM with other analytical modeling techniques applicable to resonant converters is provided in Appendix VI.

The LBSM derived waveforms can also be used to determine the boundary between full and partial ZVS for both the SRC and the PSC. Full ZVS is lost and partial ZVS starts when the absolute value of the inductor current at the instant when the leading leg switches ($\text{I}_{\text{L,sw}}$) is not large enough to fully charge/discharge the transistor output capacitances (C_{oss}) to $\text{V}_{\text{IN}}/0$ V during the dead time. As can be seen from Fig. 16(c), the absolute value of

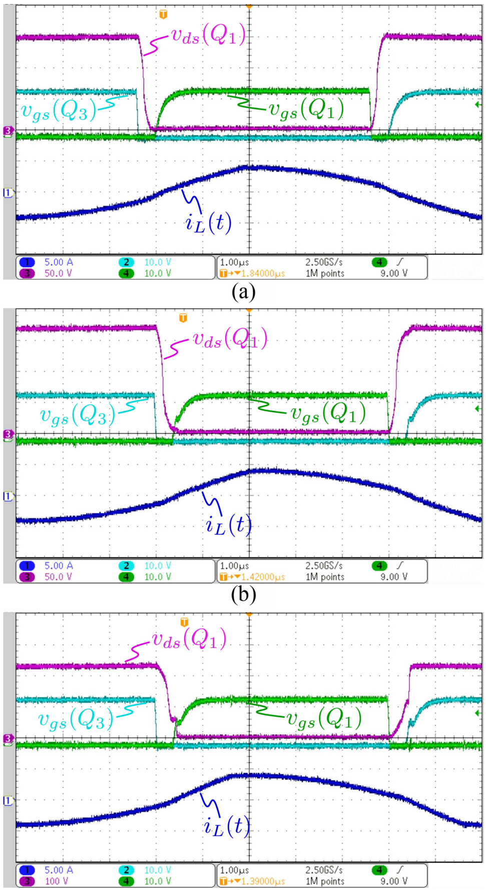

(a)

(b)

(c)

Fig. 18. Switching waveforms for the leading leg of the SRC's inverter [Q_1 and Q_3 of Fig. 10(a)] including Q_1's gate-source voltage $v_{\mathrm{gs}}(Q_1)$, Q_3's gate-source voltage $v_{\mathrm{gs}}(Q_3)$, Q_1's drain-source voltage $v_{\mathrm{ds}}(Q_1)$ and inductor current $i_{\mathrm{L}}(t)$ under different operating conditions: (a) full ZVS with $V_{\mathrm{IN}} = 150$ V, (b) boundary between full ZVS and partial ZVS with $V_{\mathrm{IN}} = 175$ V, and (c) partial ZVS with $V_{\mathrm{IN}} = 225$ V.

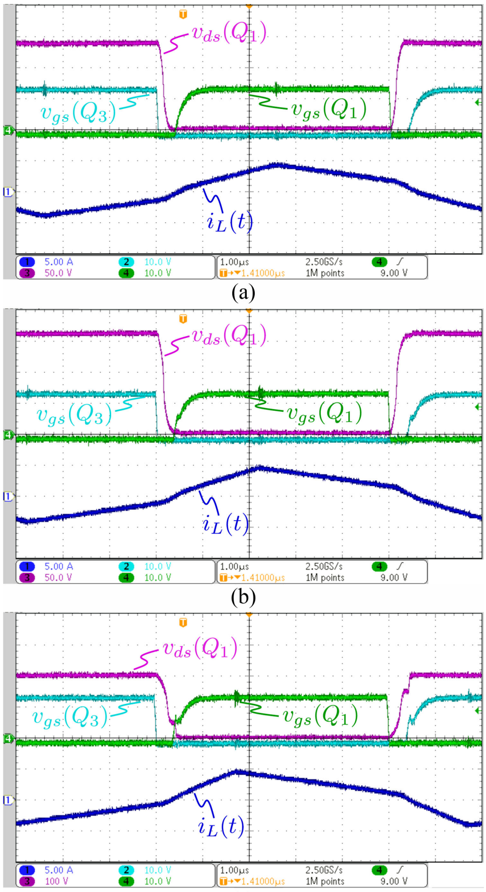

(a)

(b)

(c)

Fig. 19. Switching waveforms for the leading leg of the PSC's inverter [Q_1 and Q_3 of Fig. 10(a)] including Q_1's gate-source voltage $v_{\mathrm{gs}}(Q_1)$, Q_3's gate-source voltage $v_{\mathrm{gs}}(Q_3)$, Q_1's drain-source voltage $v_{\mathrm{ds}}(Q_1)$, and inductor current $i_{\mathrm{L}}(t)$ under different operating conditions: (a) full ZVS with $V_{\mathrm{IN}} = 140$ V, (b) boundary between full ZVS and partial ZVS with $V_{\mathrm{IN}} = 165$ V, and (c) partial ZVS with $V_{\mathrm{IN}} = 205$ V.

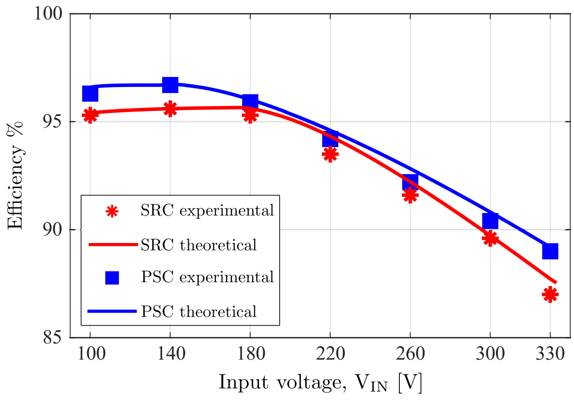

Fig. 20. Experimentally measured and theoretically calculated efficiencies for the SRC and the PSC as a function of input voltage.

$I_{\mathrm{L,sw}}$ decreases with decreasing phase shift. Using the LBSM calculated values for $I_{\mathrm{L,sw}}$ and the output capacitance data for the leading leg transistors, the phase-shifts below which full ZVS is lost and partial ZVS begins is 0.4π and 0.44π for the SRC and the PSC, respectively. These phase-shifts correspond to full ZVS being lost when input voltage exceeds 175 and 165 V for the SRC and the PSC, respectively. These threshold voltages defining the boundary between full and partial ZVS are also validated through experiment, as shown in Figs. 18 and 19. Figs. 18 and 19 show the switching waveforms for the leading legs of the SRC and the PSC, respectively, when operating at input voltages below, equal to and above these threshold voltages. As can be seen from Figs. 18(b) and 19(b), the drain-source voltage of the top transistor of the inverter's leading leg barely makes it smoothly all the way to zero and all the way back up to the input voltage when the input voltage is equal to the threshold voltage for the SRC and the PSC, respectively, indicating the boundary between full and partial ZVS.

Fig. 20 shows the measured efficiency of the prototyped SRC and the prototyped PSC for input voltages ranging from 100 to 330 V while delivering 100 W of output power at an output voltage of 40 V. The theoretically predicted efficiencies for the two converters, determined using the loss model given in Appendix V, are also shown in Fig. 20. As can be seen there is a good match between theory and experiment, and the PSC has a higher efficiency than the SRC across the full input voltage range. Given that the two converters are designed for a maximum-to-minimum input voltage ratio greater than 2, this result is expected based on the analysis presented using LBSM in Section IV. The higher efficiency of the PSC compared to the SRC is also expected since the prototyped PSC provides a larger voltage gain than the SRC across the entire phase-shift range [see Fig. 16(b)], resulting in lower primary-side conduction losses and inductor core losses in the PSC. Beyond the threshold input voltages where full ZVS is lost (175 V for SRC and 165 V for PSC), the efficiency of both converters decreases with increasing input voltage due to increased switching losses. However, the PSC maintains its efficiency advantage over the SRC even at the highest input voltage.

VI. CONCLUSION

A new approach to steady-state modeling, referred to as LBSM, has been developed and demonstrated to be an effective tool for the analysis and design of a broad class of power converters. In LBSM, the converter is first modeled using an equivalent circuit in which the switches are replaced by independent voltage or current sources whose periodic and discontinuous values may depend on the initial values of the converter's state variables during steady-state operation. The initial values of the state variables under steady-state operation are determined using the LBT. The constant-coefficient nonhomogeneous ODE associated with the equivalent circuit is then solved for one switching period to determine closed-form expressions for the converter's steady-state waveforms.

The value of LBSM is demonstrated by applying it to a number of different power converters, including the buck converter, the phase-shift controlled series resonant converter, and the phase-shift converter, which are classified as edge switch-network converters, and the boost converter operating in either CCM or DCM, which is classified as an interior switch-network converter. The LBSM derived waveforms are experimentally validated for boost converters operating in CCM and DCM. To the best of authors knowledge, LBSM is the first systematic modeling approach that can provide accurate closed-form expressions for the steady-state switched waveforms of interior switch-network converters. The technique developed to model interior switch-network converters is also applicable to edge switch-network converters, although it has steps that are not needed for edge switch-network converters. Therefore, a shorter modeling technique applicable only to edge switch-network converters is also provided. The limitations of LBSM are also identified, and ways to overcome some of these limitations are described. For example, for the modeling of converters operating in DCM, LBSM generally requires a numerical solution.

LBSM also reveals interesting facets of different converters. For example, LBSM uncovers the dependence of voltage gain on load resistance for a lossless boost converter operating in CCM, which is not predicted by small ripple approximation. The LBSM derived closed-form analytical expressions for the phase-shift controlled SRC and the PSC are also used to design and compare these converters. By comparing their ZVS boundaries, the preferred operating ranges for the SRC and the PSC are determined. It is discovered that if the required maximum-to-minimum converter input voltage ratio is less than two, then the SRC has better performance, otherwise the PSC is superior. The converter voltage gains, ZVS ranges, and efficiencies for the SRC and the PSC predicted by LBSM are validated using experimental prototypes.

APPENDIX I
PROOF OF LBT

This appendix provides a rigorous proof of the LBT. The proof of LBT relies on the properties of periodic functions and two other theorems, which are described and proved first.

A. *Periodic Functions*

Let f be a function on $(0, \infty)$ for which there is a constant $\sigma_0 \in R$ such that $\int_0^\infty e^{-\sigma_0 t}|f(t)|\,dt < \infty$. In particular, f can be piecewise smooth, consist of an infinite sequence of Dirac functions, or be a linear combination of both, as in these situations the condition is fulfilled. Then, the Laplace transform of f is defined by

$$F(s) = (\mathcal{L}f)(s) := \int_0^\infty e^{-st} f(t)\,dt \tag{A-1}$$

on the half plane $\Re s > \sigma_0$ and represents an analytic function there. Under certain conditions, F extends to a larger domain as a meromorphic function. One such possibility relates to periodic functions, as described below.

Let f be integrable over $[0, \mathrm{T})$, where $\mathrm{T} > 0$, and extend f periodically over $[0, \infty)$. We denote the family of all such functions by $\mathcal{P}_T$. As a common prototype, f can be the linear combination of a piecewise smooth function and a finite number of Dirac functions on $[0, \mathrm{T})$. Using (A-1) and a geometric series argument, it is easy to see that the Laplace transform of f is given by [25]

$$F(s) = \frac{1}{1 - e^{-s\mathrm{T}}} \int_{[0,\mathrm{T})} e^{-st} f(t)\,dt. \tag{A-2}$$

We hesitate to write $\int_0^{\mathrm{T}}$ because if there is a Dirac function anchored at point $t = 0$, then by periodicity it appears again at $t = \mathrm{T}$. However, it must be counted only once in (A-2). To avoid such a potential problem, in the following whenever we write $\int_a^b$ we mean $\int_{[a,b)}$.

The function F is initially defined in the right-half plane $\Re s > 0$, i.e., $\sigma_0 = 0$. This condition is imposed to guarantee the convergence of the geometric series, which creates the factor $1/(1 - e^{-s\mathrm{T}})$. But, using the formula (A-2), we can extend it to a meromorphic function on the whole complex plane $\mathbb{C}$ with simple poles on the imaginary axis: $p_n = i\frac{2n\pi}{\mathrm{T}}$, $n \in \mathbb{Z}$, the set of all integers. In particular, if there is no factor of the form s^n, $n \geq 1$, in the denominator, the origin is always a simple pole of F. This necessary condition plays a vital role in the "only if" part of the LBT. Let us state this result as a lemma for further reference (see [25], [26]).

Lemma 1: Let F be the Laplace transform of the function f. Assume that F has either multiple poles, or poles, which are not on the imaginary axis. Then, f is not periodic.

If F is given by (A-2), P and Q are polynomials, and we consider the combination $G := \frac{F-Q}{P}$, then $g = \mathcal{L}^{-1}(G)$ is not necessarily periodic over $(0, \infty)$. Almost all the time, there are exponential terms, which are created due to the zeros of P. However, based on the abovementioned discussion, we find a necessary and sufficient condition, which ensures the periodicity of g. The condition also reveals that the periodicity is a very rare situation.

B. Quotient Operator

Assume that function $F(s)$ is analytic in a neighborhood of the point a. Then, the quotient operator Q_a is defined by

$$(Q_aF)(s) := \frac{F(s) - F(a)}{s-a}, \qquad (s \neq a). \tag{A-3}$$

At the point $s = a$, in order to obtain an analytic function Q_aF, we have no choice but to define

$$(Q_aF)(a) = F'(a). \tag{A-4}$$

The function Q_aF is meromorphic on the same domain that F is defined. This operator is usually used to eliminate the zeros of F. Note that if $F(a) = 0$, then Q_aF is obtained by removing the factor $s - a$ from F. If we repeat this process a finite number of times (the order of the zero), then Q_a^nF is zero free at $s = a$ (see [27]). The following result is an essential observation about periodic functions. In technical language, it says that $\mathcal{P}_T$ is invariant under the operation $\mathcal{L}^{-1}(Q_aF)$.

Theorem 1: Let $f \in \mathcal{P}_T$, and let $a \in \mathbb{C} \setminus \{j\frac{2n\pi}{T} : n \in \mathbb{Z}\}$. Then, $\mathcal{L}^{-1}(Q_aF) \in \mathcal{P}_T$.

Using elementary properties of Laplace transform [28], we see that

$$\mathcal{L}^{-1}(Q_aF)(t) = -F(a)e^{at} + e^{at}\int_0^t e^{-a\tau} f(\tau)\, d\tau, \qquad (t > 0) \tag{A-5}$$

where $F(a)$ is given by (A-2) (and, in fact, not by (A-1) if $\Re a \leq 0$). Then, for all $t > 0$

$$\begin{aligned}
\mathcal{L}^{-1}(Q_aF)(t+\mathrm{T}) &= -F(a)e^{a(t+\mathrm{T})} \\
&\quad + e^{a(t+\mathrm{T})}\int_0^{t+\mathrm{T}} e^{-a\tau} f(\tau)\, d\tau \\
&= -F(a)e^{a(t+\mathrm{T})} + e^{a(t+\mathrm{T})}\left(\int_0^{\mathrm{T}} + \int_{\mathrm{T}}^{t+\mathrm{T}}\right) e^{-a\tau} f(\tau)\, d\tau \\
&= -F(a)e^{a(t+\mathrm{T})} + e^{a(t+\mathrm{T})}\left(\int_0^{\mathrm{T}} e^{-a\tau} f(\tau)\, d\tau \right. \\
&\quad \left. + \int_0^t e^{-a(\tau+\mathrm{T})} f(\tau + T)\, d\tau\right) \\
&= -F(a)e^{a(t+\mathrm{T})} + e^{a(t+\mathrm{T})}(1 - e^{-a\mathrm{T}})F(a) \\
&\quad + e^{a(t+\mathrm{T})}e^{-a\mathrm{T}}\int_0^t e^{-a\tau} f(\tau)\, d\tau \\
&= -F(a)e^{at} + e^{at}\int_0^t e^{-a\tau} f(\tau)\, d\tau = \mathcal{L}^{-1}(Q_aF)(t).
\end{aligned}$$

In other words, $\mathcal{L}^{-1}(Q_aF)$ is periodic on $(0, \infty)$ with period T.

Theorem 1 can be extended to include the poles $a = j\frac{2n\pi}{\mathrm{T}}$. In this case, we may first define Q_a by $(Q_aF)(s) = (s-a)F(s)$ and then, with some modifications, the abovementioned proof still works.

C. Quotient Expansion

The classical partial fraction expansion theorem represents a rational function $f = Q/P$, where Q and P are polynomials, as a linear combination of simpler fractions $1/(s-p)^m$, where p is a root of P and m is at most the order of this root. For our application, we need a special expansion which resembles the partial fraction expansion, but it has a different methodology.

Theorem 2: Let P be a monic polynomial of degree n with distinct roots $s_1, \ldots, s_n$. Let F be a holomorphic function in a domain, which contains the roots of P. Let Q be the unique polynomial of degree at most $n - 1$ such that

$$Q(s_k) = F(s_k), \qquad (1 \leq k \leq n). \tag{A-6}$$

Then, there are constants $c_1, \ldots, c_n \in \mathbb{C}$ such that

$$\frac{F(s) - Q(s)}{P(s)} = \sum_{k=1}^{n} c_k \frac{F(s) - F(s_k)}{s - s_k}. \tag{A-7}$$

Consider Lagrange interpolating polynomials

$$L_k(s) := \prod_{\substack{l=1 \\ l\neq k}}^{n} \frac{s - s_l}{s_k - s_l}, \qquad (1 \leq k \leq n). \tag{A-8}$$

Then, the polynomial Q is uniquely given by the formula

$$Q(s) = \sum_{k=1}^{n} F(s_k)\, L_k(s). \tag{A-9}$$

Appealing again to the uniqueness of representation by Lagrange polynomials, we also have the well-known identity [29]

$$\sum_{k=1}^{n} L_k(s) \equiv 1. \tag{A-10}$$

Therefore,

$$\begin{aligned}
\frac{F(s) - Q(s)}{P(s)} &= \frac{1}{P(s)}\left(F(s)\sum_{k=1}^{n} L_k(s) - \sum_{k=1}^{n} F(s_k)\, L_k(s)\right) \\
&= \sum_{k=1}^{n} \frac{(F(s) - F(s_k))\, L_k(s)}{P(s)} \\
&= \sum_{k=1}^{n} \frac{F(s) - F(s_k)}{(s - s_k)\prod_{\substack{l=1 \\ l\neq k}}^{n}(s_k - s_l)} = \sum_{k=1}^{n} c_k \frac{F(s) - F(s_k)}{s - s_k}
\end{aligned}$$

where

$$c_k = \left(\prod_{\substack{l=1 \\ l\neq k}}^{n} (s_k - s_l)\right)^{-1}, \qquad (1 \leq k \leq n). \tag{A-11}$$

As a byproduct of this proof, it is interesting to see that the constants c_j do not depend on F. They are uniquely determined by the zeros of P via (A-11) (recall that P is monic; otherwise there is a multiplicative constant that should be considered).

D. Linear Systems

Consider the initial value problem

$$a_n\frac{d^nx}{dt^n}+a_{n-1}\frac{d^{n-1}x}{dt^{n-1}}+\cdots+a_0x(t)=f(t),(t>0) \tag{A-12}$$

where a_k's are complex numbers, $a_n\neq 0$, and $f\in\mathcal{P}_T$. Upon taking the Laplace transform of (A-12), we obtain

$$P(s)X(s)+Q(s)=F(s) \tag{A-13}$$

where P is the characteristic polynomial with order n and Q is a polynomial of degree at most $n-1$ formed with the initial values of the system. Therefore, solving for X, we easily see that

$$X(s)=\frac{F(s)-Q(s)}{P(s)}. \tag{A-14}$$

Assume that P has n distinct zeros, which can be everywhere in the complex plane except at the poles of F, i.e., at $p_n=j\frac{2n\pi}{\mathrm{T}}$, $n\in\mathbb{Z}$, and let a be a zero of P. If $F(a)-Q(a)\neq 0$, then X has a pole at a and, by Lemma 1, we immediately conclude that x is not a periodic function. This simple observation shows that a necessary condition for having a periodic response is that $F(a)-Q(a)=0$ at all zeros of P. However, it is not trivial at all that this condition is also sufficient. To add the obscurity, note that P and Q are polynomials while F has the factor $1-e^{-s\mathrm{T}}$. It is not clear why the assumption $F(a)-Q(a)=0$, for all zeros a, essentially forces this factor to pop out for the whole combination, e.g., as in (A-2), and thus, the inverse Laplace transform would give us a periodic function. Some deep observations from operator theory are needed to characterize the situation under which the system gets an input from $\mathcal{P}_T$ and provides an output precisely in the same space.

Laplace Based Theorem: Let $f\in\mathcal{P}_T$. Assume that the characteristic polynomial of the linear system (A-12) has n distinct roots $s_1,\ldots,s_n$ with

$$s_k\in\mathbb{C}\setminus\{j\frac{2n\pi}{\mathrm{T}}:n\in\mathbb{Z}\},\qquad(1\leq k\leq n). \tag{A-15}$$

Then, the system has a periodic solution (i.e., $x(t)\in\mathcal{P}_T$) if and only if

$$F(s_k)=Q(s_k),\qquad(1\leq k\leq n). \tag{A-16}$$

Moreover, the abovementioned conditions are fulfilled for a unique choice of initial values.

We already observed that F is meromorphic with poles on the imaginary axis. The assumption (A-15) ensures that F is analytic at the zeros of P. Thus, according to Theorem 2, there are constants $c_1,\ldots,c_n\in\mathbb{C}$ [see (A-11)] such that

$$X(s)=\frac{F(s)-Q(s)}{P(s)}=\sum_{k=1}^{n}c_j\frac{F(s)-F(s_k)}{s-s_k}. \tag{A-17}$$

Using the quotient operator Q_a, we may rewrite the abovementioned formula as

$$X(s)=\sum_{k=1}^{n}c_k(Q_{s_k}F)(s). \tag{A-18}$$

Therefore,

$$x(t)=\sum_{k=1}^{n}c_k\,\mathcal{L}^{-1}(Q_{s_k}F)(t) \tag{A-19}$$

and Theorem 1 ensures that each function $\mathcal{L}^{-1}(Q_{s_k}F)$ is periodic over $(0,\infty)$ with period T.

APPENDIX II
LBSM UNDER STATE-SPACE REPRESENTATION

This appendix describes the LBSM technique under the state-space representation of a power converter. The first step of this technique is to model the converter in the following state-space form

$$\frac{d\boldsymbol{x}}{dt}=\boldsymbol{A}\boldsymbol{x}(t)+\boldsymbol{g}(t) \tag{A-20}$$

where $\boldsymbol{x}(t)$ is the state vector (i.e., a vector of state variables), $\boldsymbol{A}$ is a constant matrix, and $\boldsymbol{g}(t)$ is a periodic and discontinuous vector. The procedure for obtaining this state-space representation depends on whether the power converter is an edge-switch network or an interior-switch network converter.

Edge-switch network converters can be modeled in the form of (A-20) by first deriving the state-space representation of the converter for each of its subintervals in the following form:

$$\frac{d\boldsymbol{x}}{dt}=\boldsymbol{A_i}\boldsymbol{x}(t)+\boldsymbol{B_i}\boldsymbol{u}(t)\quad 1\leq i\leq m \tag{A-21}$$

where $\boldsymbol{A_i}$ and $\boldsymbol{B_i}$ are constant matrices dependent on the topology of the converter, $\boldsymbol{u}(t)$ is a vector obtained from the actual or equivalent sources connected at the input and output ports of the converter, and m is the total number of subintervals. The time evolution of the state vector across all its subintervals can now be expressed as

$$\frac{d\boldsymbol{x}}{dt}=\sum_{i=1}^{m}q_i(t)\boldsymbol{A_i}\boldsymbol{x}(t)+\sum_{i=1}^{m}q_i(t)\boldsymbol{B_i}\boldsymbol{u}(t) \tag{A-22}$$

where $q_i(t)$ is a periodic and discontinuous switching function that equals 1 during the ith subinterval and 0 during all other subintervals, and satisfies $\sum_{i=1}^{m}q_i(t)=1$. In edge switch-network converters, since switching action does not reconfigure the interconnection between its energy storage elements, all $\boldsymbol{A_i}$ matrices are equal, i.e., $\boldsymbol{A_1}=\boldsymbol{A_2}=\cdots=\boldsymbol{A_m}\equiv\boldsymbol{A_0}$. However, since switching action does reconfigure the connection to the sources at the ports, the $\boldsymbol{B_i}$ matrices are not equal in all subintervals. Hence, the converter's state-space representation can be simplified to

$$\frac{d\boldsymbol{x}}{dt}=\boldsymbol{A_0}\boldsymbol{x}(t)+\sum_{i=1}^{m}q_i(t)\boldsymbol{B_i}\boldsymbol{u}(t). \tag{A-23}$$

This has the desired form of (A-20), where $\boldsymbol{A}=\boldsymbol{A_0}$ and $\boldsymbol{g}(t)=\sum_{i=1}^{m}q_i(t)\boldsymbol{B_i}\boldsymbol{u}(t)$.

To model interior switch-network converters in the form of (A-20) an extra initial step must be included. This step determines an analytical expression for the state vector $\boldsymbol{x}(t)$ in terms of its unknown steady-state initial value $\boldsymbol{X_0}$ using the following equation by starting with the first subinterval [8]:

$$\boldsymbol{x}(t) = \left(\boldsymbol{X_{i-1}} e^{\boldsymbol{A_i}(t-t_{i-1})} + \int_{t_{i-1}}^{t} e^{\boldsymbol{A_i}\tau} \boldsymbol{B_i} \boldsymbol{u}(t-\tau) d\tau\right), \ t_{i-1} \leq t \leq t_i \quad \text{(A-24)}$$

where $\boldsymbol{X_{i-1}}$ is the value of the state vector at the beginning of the ith subinterval (which for $i \geq 2$ is known from the previous subinterval), t_{i-1} is the total time elapsed until the beginning of the ith subinterval, $\boldsymbol{A_i}$ and $\boldsymbol{B_i}$ are converter matrices for the ith subinterval as defined in (A-21). Next, the state-space representation of the converter for each of its subintervals in the same form as (A-21) must be derived and used to express the time evolution of the state vector across all subintervals in the same form as (A-22). In interior switch-network converters, since switching action reconfigures the interconnection between its energy storage elements, the $\boldsymbol{A_i}$ matrices are not equal in all subintervals. Also the $\boldsymbol{B_i}$ matrices are not equal. Rewriting $\sum_{i=1}^{m} q_i(t) = 1$ as $q_m(t) = 1 - \sum_{i=1}^{m-1} q_i(t)$, the converter's state-space representation can be expressed as

$$\frac{d\boldsymbol{x}}{dt} = \boldsymbol{A_m}\boldsymbol{x}(t) + \sum_{i=1}^{m-1} q_i(t)\left(\boldsymbol{A_i} - \boldsymbol{A_m}\right)\boldsymbol{x}(t) + \sum_{i=1}^{m} q_i(t)\boldsymbol{B_i}\boldsymbol{u}(t). \quad \text{(A-25)}$$

Utilizing (A-24) to eliminate $\boldsymbol{x}(t)$ from the second right-hand-side term of (A-25), and defining $\boldsymbol{\Psi}(t)$ as

$$\boldsymbol{\Psi}(t) \equiv \sum_{i=1}^{m-1} q_i(t)\left(\boldsymbol{A_i} - \boldsymbol{A_m}\right)\left(\boldsymbol{X_{i-1}} e^{\boldsymbol{A_i}(t-t_{i-1})} + \int_{t_{i-1}}^{t} e^{\boldsymbol{A_i}\tau}\boldsymbol{B_i}\boldsymbol{u}(t-\tau)d\tau\right) \quad \text{(A-26)}$$

transforms the converter's state-space representation to

$$\frac{d\boldsymbol{x}}{dt} = \boldsymbol{A_m}\boldsymbol{x}(t) + \boldsymbol{\Psi}(t) + \sum_{i=1}^{m} q_i(t)\boldsymbol{B_i}\boldsymbol{u}(t). \quad \text{(A-27)}$$

This has the desired form of (A-20), where $\boldsymbol{A} = \boldsymbol{A_m}$ and $\boldsymbol{g}(t) = \boldsymbol{\Psi}(t) + \sum_{i=1}^{m} q_i(t)\boldsymbol{B_i}\boldsymbol{u}(t)$. It is interesting to note that edge switch-network converters are a special case of interior switch-network converters, as (A-27) reduces to (A-23) when all $\boldsymbol{A_i}$ matrices are the same (and defined equal to $\boldsymbol{A_0}$). Once the power converter has been modeled in the form of (A-20), steps similar to those described in Section II-A can be used to derive an equation analogous to (5)

$$\boldsymbol{X_0} = -\left[\boldsymbol{I} - e^{-\boldsymbol{A}\mathrm{T}}\right]^{-1} \int_{0}^{\mathrm{T}} e^{-\boldsymbol{A}t}\boldsymbol{g}(t)dt \quad \text{(A-28)}$$

where the initial value of the state vector under steady-state operation $\boldsymbol{X_0}$ is analogous to $[x(0), x'(0), \ldots, x^{(n-1)}(0)]$ in (5). In the case of edge-switch network converters, $\boldsymbol{X_0}$ can be determined explicitly from (A-28) since all the terms on the right-hand-side of the equation are known. In the case of interior-switch network converters, $\boldsymbol{g}(t)$ is a function of $\boldsymbol{X_0}$ making (A-28) an implicit equation in $\boldsymbol{X_0}$. However, (A-28) is still linear and can be used to solve for $\boldsymbol{X_0}$. Once $\boldsymbol{X_0}$ is known, (A-20) can be solved to find the steady-state solution for $\boldsymbol{x}(t)$ across one switching period.

APPENDIX III
APPLICATION OF LBSM TO DC–AC AND AC–DC CONVERTERS

This appendix demonstrates the application of LBSM to two dc–ac converters, one of which is bidirectional and can also be considered as an ac–dc converter. As an example of a dc–ac converter in which its steady-state waveforms are periodic with a period equal to its switching period, consider the series resonant inverter shown in Fig. 21(a), which is commonly used for induction heating applications. An ODE for this converter can be derived using steps (M1) and (M2) of LBSM for edge-switch network converters

$$\mathrm{LC}\frac{d^2 v_{\mathrm{C}}}{dt^2} + \mathrm{RC}\frac{dv_{\mathrm{C}}}{dt} + v_{\mathrm{C}}(t) = v_i(t) \quad \text{(A-29)}$$

where $v_i(t)$ is the rectangular switch node waveform. This ODE is similar to (6), but with different roots for its characteristic polynomial

$$s_{1,2} = \frac{R}{2\mathrm{L}}\left(-1 \pm \sqrt{1 - 4\frac{\mathrm{L}}{\mathrm{R}^2\mathrm{C}}}\right) \equiv s_r \pm s_m. \quad \text{(A-30)}$$

Following steps (S1) through (S4) for (A-29), the steady-state capacitor voltage is identical to the expression given by (11) except with the values of s_r and s_m replaced by those given in (A-30). The inductor current can be obtained by differentiating (11). The LBSM predicted capacitor voltage and inductor current waveforms for an example series resonant inverter are compared with PSIM simulations in Fig. 21(b) and (c), which show a good match between the LBSM predicted and the simulated waveforms.

As an example of a dc–ac converter in which its steady-state waveforms are periodic with a period equal to the period of a more slowly varying external ac voltage, consider the bidirectional line-interfaced high-frequency dc–ac converter shown in Fig. 22(a). Here, the line voltage is represented by a sinusoidal ac voltage source $v_g(t)\ (= \mathrm{V}_g \sin(2\pi f_g t - \phi_g))$ with amplitude V_g, frequency f_g, and phase ϕ_g. The switching frequency of the converter is f_s, and the converter uses a unipolar sinusoidal PWM signal $m(t)\ (= m_a \sin(2\pi f_g t))$ with an amplitude modulation ratio $m_a\ (0 \leq m_a \leq 1)$ and a frequency modulation ratio $m_f (= \frac{f_s}{f_g})$. The PWM is implemented digitally with $m(t)$ discretized in time at a frequency of $2f_s$. An ODE for this converter can be derived using steps (M1) and (M2) of LBSM for edge-switch network converters

$$\mathrm{L}\frac{di_{\mathrm{L}}}{dt} = v_i(t) - v_g(t) \equiv f(t) \quad \text{(A-31)}$$

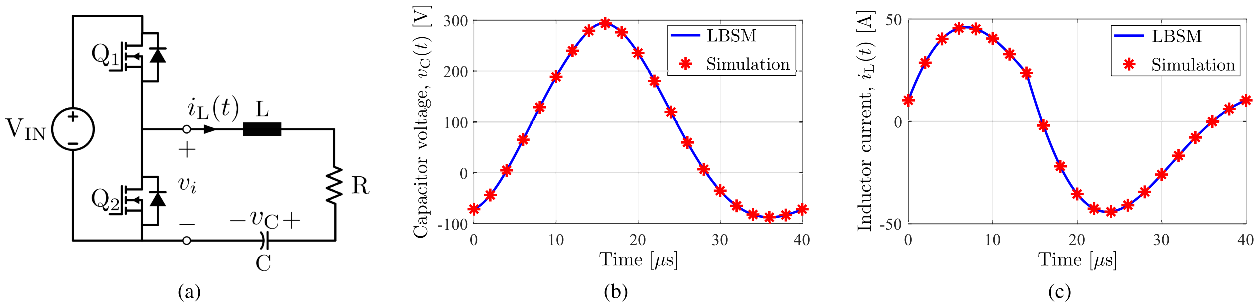

(a) (b) (c)

Fig. 21. Series resonant inverter: (a) topology, and comparison of its (b) capacitor voltage (v_C) and (c) inductor current (i_L) waveforms, obtained using LBSM and PSIM simulation with the following parameter values: $V_{IN} = 230$ V, $L = 25\ \mu$H, $C = 1.44\ \mu$F, $R = 3\ \Omega$, $f_s = 25$ kHz, and $D = 0.35$.

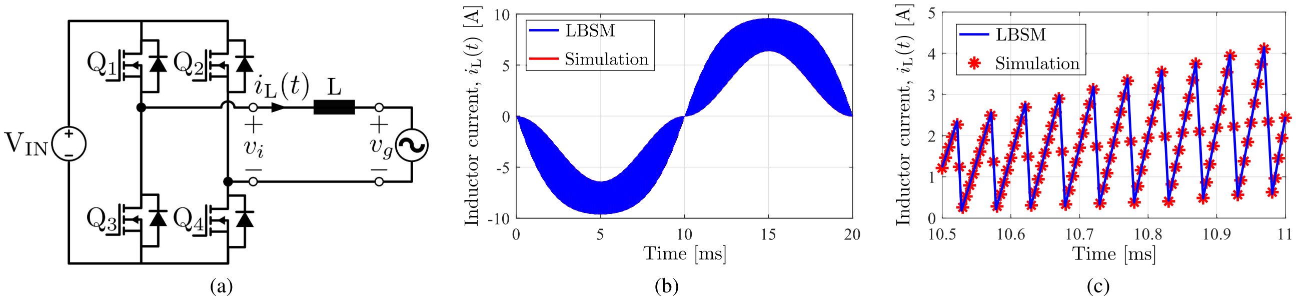

(a) (b) (c)

Fig. 22. Bidirectional line-interfaced high-frequency dc–ac converter: (a) topology, and comparison of its inductor current (i_L) waveforms across (b) a full line-cycle and (c) five switching cycles, obtained using LBSM and PSIM simulation with the following parameter values: $f_s = 10$ kHz, $f_g = 50$ Hz, $m_a = 0.8$, $V_{IN} = 400$ V, $V_g = 320$ V, and $\phi_g = 0$.

where $v_i(t)$ is the rectangular waveform generated by the full bridge. Assuming that the period of $v_g(t)$ is an integer multiple of the switching period (i.e., the frequency modulation ratio m_f is an integer), the input $f(t)$ will be periodic with frequency f_g. To determine the converter's steady-state waveforms from this ODE, first $F(s) = \mathcal{L}\{v_i(t) - v_g(t)\}$ is determined following (S1); next following (S2), the root of the characteristic polynomial $P(s)$ $(= Ls)$ is found to be $s = 0$; then formulating $Q(s = 0) = F(s = 0)$ following (S3) and solving it gives the steady-state initial condition for the inductor current:

$$i_L(0) = \frac{V_g}{\omega_g L}\cos(\phi_g) - \frac{m_a V_{IN}}{\omega_g L}\frac{\pi}{2m_f}\sum_{n=0}^{m_f-1}\sin\left(n\frac{\pi}{m_f}\right) \tag{A-32}$$

where $\omega_g = 2\pi f_g$. Finally, solving (A-31) across one line-period (i.e., $1/f_g$) results in

$$\begin{aligned} i_L(t) = i_L(0) + \frac{V_g}{\omega_g L}\cos(\phi_g) - \frac{V_g}{\omega_g L}\cos(\omega_g t - \phi_g) \\ + \frac{V_{IN}}{L}\sum_{n=0}^{m_f-1} r(t - t_{\min}) - r(t - t_{\max}) \end{aligned} \tag{A-33}$$

where $t_{\min} = \frac{1}{2f_s}(n + 0.5 - 0.5m_a\sin(n\frac{\pi}{m_f}))$ and $t_{\max} = \frac{1}{2f_s}(n + 0.5 + 0.5m_a\sin(n\frac{\pi}{m_f}))$ and $r(t - t_0)$ is a ramp function starting at t_0 as defined in the following:

$$r(t - t_0) = \begin{cases} t - t_0 & t \geq t_0 \\ 0 & t < t_0. \end{cases} \tag{A-34}$$

The LBSM predicted inductor current waveform for an example bidirectional line-interfaced high-frequency dc–ac converter is compared with PSIM simulation across a full line cycle in Fig. 22(b) and across five switching cycles in Fig. 22(c). As can be seen there is an excellent match between the LBSM predicted and the simulated waveforms.

APPENDIX IV
EFFECTIVE PHASE SHIFT FOR SRC AND PSC TO ACCOUNT FOR INVERTER DEAD TIME

For both the SRC and the PSC assuming full or partial ZVS, during the dead time of a half-bridge, the dominant resonance is between the converter's inductor L and the output capacitors (C_{oss}) of that half-bridge's two transistors (which act as if in parallel). Any other capacitors of the converter (e.g., the tank capacitor C in the case of the SRC) have little impact on this resonance as they are much larger than, and appear in series with, 2˜C_{oss}. This resonance continues until the transistor output capacitors are charged/discharged to $V_{IN}/0$ V and the antiparallel diodes clamp their voltages, or the inductor current changes direction. This resonance occurs during the dead times of both the leading and the lagging half-bridges, and results in a change in the volt-seconds applied by the inverter in a half switching period. However, the impact on inverter volt-seconds due to the dead time of the lagging half-bridge is much smaller than that of the leading half-bridge, as the lagging half-bridge switches at a much higher current resulting in a much smaller inverter output voltage transition time. Hence, the impact of the dead time of the lagging half-bridge is neglected in this analysis. Considering the radial half time period $0 \leq \omega_s t < \pi$, the instantaneous output voltage of the inverter v_i during the dead time of the leading half-bridge is given by

$$v_i = \mathrm{Z_{oss}I_{L,sw}} \sin\left(\omega_{\mathrm{oss}}t - \frac{\omega_{\mathrm{oss}}}{\omega_{\mathrm{s}}}\frac{\pi-\phi}{2}\right) \qquad \text{(A-35)}$$

where $\omega_{\mathrm{oss}}(\equiv \frac{1}{\sqrt{2\mathrm{LC_{oss}}}})$ and $\mathrm{Z_{oss}}(\equiv \sqrt{\frac{\mathrm{L}}{2\mathrm{C_{oss}}}})$ are the resonant frequency and the characteristic impedance of the tank formed by L and $2\mathrm{C_{oss}}$, respectively, $\frac{\pi-\phi}{2}$ is the radial time when the leading half-bridge starts to switch, and $\mathrm{I_{L,sw}}$ is the inductor current at the instant $\frac{\pi-\phi}{2}$. The value of $\mathrm{I_{L,sw}}$ used here is determined using LBSM without considering dead times as a reasonably good approximation. The time it takes for the inverter output voltage to reach $\mathrm{V_{IN}}$, Δt, can be determined from (A-35) if $\mathrm{Z_{oss}I_{L,sw}}$ is greater than or equal to $\mathrm{V_{IN}}$, otherwise, the time taken is the full dead time t_{d} at which point the transistor output capacitors are hard charged; hence, Δt is given by

$$\Delta t = \begin{cases} \frac{1}{\omega_{\mathrm{oss}}}\sin^{-1}\left(\frac{\mathrm{V_{IN}}}{\mathrm{Z_{oss}I_{L,sw}}}\right) & \text{if } \mathrm{Z_{oss}I_{L,sw}} \geq \mathrm{V_{IN}} \\ t_{\mathrm{d}} & \text{if } \mathrm{Z_{oss}I_{L,sw}} < \mathrm{V_{IN}} \end{cases} \qquad \text{(A-36)}$$

which is the same as (49). The average value of the inverter output voltage during the dead time is given by

$$\begin{aligned} \mathrm{V}_{i,\mathrm{d}} &= \frac{1}{t_{\mathrm{d}}}\left(\int_0^{\Delta t} \mathrm{Z_{oss}I_{L,sw}}\sin(\omega_{\mathrm{oss}}t)dt + \int_{\Delta t}^{t_{\mathrm{d}}} \mathrm{V_{IN}}dt\right) \\ &= \frac{1}{t_{\mathrm{d}}}\left(\frac{\mathrm{Z_{oss}I_{L,sw}}}{\omega_{\mathrm{oss}}}\left(1-\cos(\omega_{\mathrm{oss}}\Delta t)\right) + \mathrm{V_{IN}}\left(t_{\mathrm{d}}-\Delta t\right)\right). \end{aligned} \qquad \text{(A-37)}$$

The dead time eats into the duration ϕ when the inverter output voltage is $\mathrm{V_{IN}}$. Hence, an effective phase shift ϕ_{eff} can be defined for a dead-time-free inverter such that the volt-seconds delivered by it are equal to the actual volt-seconds delivered by the inverter with a dead time

$$\phi_{\mathrm{eff}}\mathrm{V_{IN}} = (\phi - \omega_{\mathrm{s}}t_{\mathrm{d}})\,\mathrm{V_{IN}} + \omega_{\mathrm{s}}t_{\mathrm{d}}\mathrm{V}_{i,\mathrm{d}}. \qquad \text{(A-38)}$$

Substituting for $\mathrm{V}_{i,\mathrm{d}}$ from (A-37) into (A-38) and solving for ϕ_{eff} gives

$$\phi_{\mathrm{eff}} = \phi - \omega_{\mathrm{s}}\left(\Delta t - \frac{\mathrm{Z_{oss}I_{L,sw}}}{\omega_{\mathrm{oss}}\mathrm{V_{IN}}}\left(1-\cos(\omega_{\mathrm{oss}}\Delta t)\right)\right) \qquad \text{(A-39)}$$

which is the same as (48). Since the SRC and the PSC operate symmetrically across a half time period, (A-39) is also the expression for effective phase shift during the second half time period ($\pi \leq \omega_{\mathrm{s}}t < 2\pi$).

APPENDIX V
LOSS MODELS FOR THE SRC AND THE PSC

This appendix provides the loss models used to predict the efficiency of the SRC and the PSC. Efficiency is calculated using $\eta = \frac{\mathrm{P_{OUT}}}{\mathrm{P_{OUT}+P_{LOSS}}}$, where $\mathrm{P_{OUT}}$ is the output power of the converter, and $\mathrm{P_{LOSS}}$ is the total loss in the converter, comprising conduction losses, transistor switching losses, and magnetic core losses. Conduction losses are calculated using

$$\mathrm{P_{COND}} = \mathrm{I_{rms}^2}\left(2\mathrm{R_{ON}} + \mathrm{R_L} + \mathrm{R_T}\right) + 2\mathrm{V_F}\frac{\mathrm{P_{OUT}}}{\mathrm{V_{OUT}}} \qquad \text{(A-40)}$$

where $\mathrm{I_{rms}}$ is the rms value of the inductor current determined from the LBSM derived inductor current waveform, $\mathrm{R_{ON}}$ is the ON-resistance of the transistors, $\mathrm{R_L}$ is the ac winding resistance of the inductor, $\mathrm{R_T}$ is the total ac winding resistance of the transformer reflected to its primary side, $\mathrm{V_F}$ is the forward voltage of the diodes, and $\mathrm{V_{OUT}}$ is the output voltage of the converter. Transistor switching losses are assumed to be zero when the converter achieves full ZVS. Under partial ZVS of the inverter's leading leg, switching losses are calculated by accounting for capacitive discharge loss and overlap loss for that leg

$$\mathrm{P_{SW}} = \mathrm{C_{oss,eq}}\mathrm{V_{RM}}^2 f_{\mathrm{s}} + \mathrm{t_{ON}}\mathrm{V_{RM}}\mathrm{I_{L,d}}f_s \qquad \text{(A-41)}$$

where $\mathrm{C_{oss,eq}}$ is the energy equivalent output capacitance of the transistor, $\mathrm{V_{RM}}$ is the switch-node voltage that remains to be discharged/charged determined using the approach described in Appendix III, f_{s} is the switching frequency, $\mathrm{t_{ON}}$ is the transistor turn-ON time, and $\mathrm{I_{L,d}}$ is the inductor current at the end of dead time determined from the LBSM derived inductor current waveform. Magnetic core losses are calculated using Steinmetz's equation

$$\mathrm{P_{CORE}} = \mathrm{C_m}f_{\mathrm{s}}^{\alpha}\left(\left(\frac{\lambda_{\mathrm{L}}}{2\mathrm{A_{e,L}N_L}}\right)^{\beta}\mathrm{V_{e,L}} + \left(\frac{\lambda_{\mathrm{T}}}{2\mathrm{A_{e,T}N_T}}\right)^{\beta}\mathrm{V_{e,T}}\right) \qquad \text{(A-42)}$$

where $\mathrm{C_m}$, α, and β are core material related constants, $\lambda_{\mathrm{T}}(=\frac{\mathrm{V_{OUT}}}{2\mathrm{f_s}})$ is the flux-linkage applied across the transformer's secondary winding, $\lambda_{\mathrm{L}}(=\mathrm{L}\Delta\mathrm{I_{L,pp}})$ is the flux-linkage applied across inductor L with peak-to-peak current $\Delta\mathrm{I_{L,pp}}$, $\mathrm{A_{e,L}}$ (and $\mathrm{A_{e,T}}$), and $\mathrm{V_{e,L}}$ (and $\mathrm{V_{e,T}}$) are the equivalent cross-sectional area and core volume, respectively, for the inductor (and the transformer), $\mathrm{N_L}$ is the number of turns in the inductor winding, and $\mathrm{N_T}$ is the number turns in the secondary winding of the transformer. The transistor, diode and magnetic core parameters used in (A-40)–(A-42) are obtained from manufacturer datasheets, and the remaining parameters are from the information in Table III.

APPENDIX VI
COMPARISON OF LBSM WITH EXISTING ANALYTICAL MODELING TECHNIQUES

This appendix compares LBSM with existing analytical techniques for modeling the steady-state waveforms of resonant converters, as summarized in Table IV. The FHA technique is the least complex, but also the least accurate; it is especially inaccurate for converters with low loaded quality factor resonant tanks and does not model DCM operation. Extensions of FHA, such as in [30] and [31], have also been developed in which the rectifier is modeled using a complex impedance instead of a resistance as in FHA. These approaches increase the modeling accuracy to some extent but at the cost of increased modeling complexity and are still unable to model DCM operation. Techniques that incorporate higher order harmonics, such as the generalized

TABLE IV
COMPARISON OF LBSM WITH EXISTING ANALYTICAL METHODS FOR MODELING STEADY-STATE WAVEFORMS OF RESONANT CONVERTERS

Method	Closed-form	Accuracy	DCM	$\phi \neq \pi$	High-order topologies	Complexity
FHA	Yes	Medium	No	Yes	Yes	Low
FHA Extensions	Yes	Low	No	Yes	Yes	Medium
GAM	No	Medium	Yes	Yes	Yes	High
SPA	Yes	High	No	No	No	High
Cyclic Averaging	Yes	Medium	No	No	Yes	High
LBSM	Yes	High	Yes	Yes	Yes	High

averaging method [12] and other similar techniques [32], also improve the modeling accuracy to a level limited by the number of harmonics that can be practically included. However, these techniques have high complexity and do not yield closed-form expressions for converter waveforms. The state plane analysis (SPA) technique, while accurate, is not practical for converters with more than two state variables, and in the case of the SRC, SPA yields closed-form expressions only if the inverter output voltage waveform is a symmetrical square wave $(\phi = \pi)$. Another analytical approach, cyclic averaging [33], uses augmented averaging matrices to determine steady-state waveforms, but requires knowledge of subinterval duration, which is determined by first applying FHA, limiting its accuracy. As can be seen from Table IV, LBSM brings a unique ability to accurately model a broad class of resonant converters without being any more complex than the existing techniques.

REFERENCES

[1] J. Sun and H. Grotstollen, "Symbolic analysis methods for averaged modeling of switching power converters," *IEEE Trans. Power Electron.*, vol. 12, no. 3, pp. 537–546, May 1997.

[2] R. Webster and K. D. T. Ngo, "Computer-based symbolic circuit analysis and simulation," in *Proc. IEEE Appl. Power Electron. Conf. Expo.*, Boston, MA, USA, Feb. 1992, pp. 772–779.

[3] N. Mohan, W. P. Robbins, T. M. Undeland, R. Nilssen, and O. Mo, "Simulation of power electronic and motion control systems-an overview," *Proc. IEEE*, vol. 82, no. 8, pp. 1287–1302, Aug. 1994.

[4] D. Maksimovic, A. M. Stankovic, V. J. Thottuvelil, and G. C. Verghese, "Modeling and simulation of power electronic converters," *Proc. IEEE*, vol. 89, no. 6, pp. 898–912, Jun. 2001.

[5] R. J. Dirkman, "The simulation of general circuits containing ideal switches," in *Proc. IEEE Power Electron. Special. Conf.*, Blacksburg, VA, USA, Jun. 1987, pp. 185–194.

[6] T. J. Aprille and T. N. Trick, "Steady-state analysis of nonlinear circuits with periodic inputs," *Proc. IEEE*, vol. 60, no. 1, pp. 108–114, Jan. 1972.

[7] D. Maksimovic, "Automated steady-state analysis of switching power converters using a general-purpose simulation tool," in *Proc. IEEE Power Electron. Special. Conf.*, Saint Louis, MO, USA, Jun. 1997, vol. 2, pp. 1352–1358.

[8] H. R. Visser and P. P. J. van denBosch, "Modelling of periodically switching networks," in *Proc. IEEE Power Electron. Special. Conf.*, Cambridge, MA, USA, Jun. 1991, pp. 67–73.

[9] A. Kumar, J. Lu, and K. K. Afridi, "Enhanced-accuracy augmented state-space approach to steady-state modeling of resonant converters," in *Proc. IEEE Workshop Control Model. Power Electron.*, Vancouver, BC, Canada, Jul. 2015, pp. 1–6.

[10] R. D. Middlebrook and S. Cuk, "A general unified approach to modelling switching-converter power stages," in *Proc. IEEE Power Electron. Special. Conf.*, Cleveland, OH, USA, Jun. 1976, pp. 18–34.

[11] C. K. Tse and M. D. Bernardo, "Complex behavior in switching power converters," *Proc. IEEE*, vol. 90, no. 5, pp. 768–781, May 2002.

[12] S. R. Sanders, J. M. Noworolski, X. Z. Liu, and G. C. Verghese, "Generalized averaging method for power conversion circuits," *IEEE Trans. Power Electron.*, vol. 6, no. 2, pp. 251–259, Apr. 1991.

[13] X. Liu, A. M. Cramer, and F. Pan, "Generalized average method for time-invariant modeling of inverters," *IEEE Trans. Circuits Syst. I*, vol. 64, no. 3, pp. 740–751, Mar. 2017.

[14] M. Esparza, J. Segundo-Ramírez, J. B. Kwon, X. Wang, and F. Blaabjerg, "Modeling of VSC-based power systems in the extended harmonic domain," *IEEE Trans. Power Electron.*, vol. 32, no. 8, pp. 5907–5916, Aug. 2017.

[15] J. Riedel, D. G. Holmes, B. P. McGrath, and C. Teixeira, "ZVS soft switching boundaries for dual active bridge DC DC converters using frequency domain analysis," *IEEE Trans. Power Electron.*, vol. 32, no. 4, pp. 3166–3179, Apr. 2017.

[16] R. L. Steigerwald, "A comparison of half-bridge resonant converter topologies," *IEEE Trans. Power Electron.*, vol. 3, no. 2, pp. 174–182, Apr. 1988.

[17] K. D. T. Ngo, "Analysis of a series resonant converter pulse width-modulated or current-controlled for low switching loss," *IEEE Trans. Power Electron.*, vol. 3, no. 1, pp. 55–63, Jan. 1988.

[18] H.-J. Jiang, G. Maggetto, and P. Lataire, "Steady-state analysis of the series resonant DC-DC converter in conjunction with loosely coupled transformer-above resonance operation," *IEEE Trans. Power Electron.*, vol. 14, no. 3, pp. 469–480, May 1999.

[19] R. Oruganti and F. C. Lee, "Resonant power processors, part i-state plane analysis," *IEEE Trans. Ind. Appl.*, vol. IA- 21, no. 6, pp. 1453–1460, Nov. 1985.

[20] W. Feng, F. C. Lee, and P. Mattavelli, "Optimal trajectory control of burst mode for llc resonant converter," *IEEE Trans. Power Electron.*, vol. 28, no. 1, pp. 457–466, Jan. 2013.

[21] J. Lu, A. Kumar, and K. K. Afridi, "A step-superposition-based analysis approach to modeling resonant converters," *IEEE Trans. Power Electron.*, vol. 33, no. 8, pp. 7148–7165, Aug. 2018.

[22] M. Daryaei, M. Ebrahimi, and S. A. Khajehoddin, "Accurate parametric steady state analysis and design tool for DC-DC power converters," in *Proc. IEEE Appl. Power Electron. Conf. Expo.*, Long Beach, CA, USA, Mar. 2016, pp. 2579–2586.

[23] M. Daryaei, M. Ebrahimi, and S. A. Khajehoddin, "Alternative approach to analysis and design of series resonant converter at steady state," *IEEE Trans. Ind. Electron.*, vol. 66, no. 6, pp. 4424–4435, Jun. 2019.

[24] Y. K. Lo, C. Y. Lin, M. T. Hsieh, and C. Y. Lin, "Phase-shifted full-bridge series-resonant DC-DC converters for wide load variations," *IEEE Trans. Ind. Electron.*, vol. 58, no. 6, pp. 2572–2575, Jun. 2011.

[25] L. Debnath and D. Bhatta, *Integral Transforms and Their Applications*. Boca Raton, FL, USA: CRC Press, 2014.

[26] G. Doetsch, *Introduction to the Theory and Application of the Laplace Transformation*. Berlin, Germany: Springer Science and Business Media, 2012.

[27] E. Fricain and J. Mashreghi, *The Theory of H. (b) Spaces*. vol. 1. Cam., U.K.: Cambridge Univ. Press, 2016.

[28] A. D. Polyanin and A. V. Manzhirov, *Handbook of Integral Equations*. Boca Raton, FL, USA: CRC Press, 2008.

[29] E. Meijering, "A chronology of interpolation: From ancient astronomy to modern signal and image processing," *Proc. IEEE*, vol. 90, no. 3, pp. 319–342, Aug. 2002.

[30] J. Martin-Ramos, J. Diaz, A. Pernia, J. Lopera, and F. Nuno, "Dynamic and steady-state models for the PRC-LCC resonant topology with a capacitor as output filter," *IEEE Trans. Ind. Electron.*, vol. 54, no. 4, pp. 2262–2275, Aug. 2007.

[31] A. J. Forsyth, G. Ward, and S. V. Mollov, "Extended fundamental frequency analysis of the LCC resonant converter," *IEEE Trans. Power Electron.*, vol. 18, no. 6, pp. 1286–1292, Nov. 2003.

[32] A. Bhat, "A generalized steady-state analysis of resonant converters using two-port model and fourier-series approach," *IEEE Trans. Power Electron.*, vol. 13, no. 1, pp. 142–151, Jan. 1998.

[33] M. P. Foster, H. I. Sewell, C. M. Bingham, D. A. Stone, D. Hente, and D. Howe, "Cyclic-averaging for high-speed analysis of resonant converters," *IEEE Trans. Power Electron.*, vol. 18, no. 4, pp. 985–993, Jul. 2003.

Mohammad Daryaei (Student Member, IEEE) received the B.Sc. degree in electrical engineering from Amirkabir University of Technology, Tehran, Iran, in 2014, and the M.Sc. degree in electrical engineering in 2016 from the University of Alberta, Edmonton, AB, Canada, where he is currently working toward the Ph.D. degree in design of dc–dc converters for renewable energy resources.

His research interests include modeling and analysis of power electronics converters, design of high-frequency power converters, soft switching converters, and dc–dc converters.

S. Ali Khajehoddin (Senior Member, IEEE) received the B.Sc. and M.Sc. degrees in electrical engineering from the Isfahan University of Technology, Isfahan, Iran, in 1997 and 2000, respectively, and the Ph.D. degree in electrical engineering specializing in power electronics and their applications in renewable energy systems from Queens University, Kingston, ON, Canada, in 2010.

After completing his master's, he cofounded a start-up company, which was focused on the development and production of power analyzers and smart metering products used for smart grid applications. For his doctoral research with Queen's University, he focused on the design and implementation of compact and durable microinverters for photovoltaic grid-connected systems. Based on this research, Queen's University spun off SPARQ systems, Inc., where, as the Lead R&D Engineer, he worked toward massproduction and commercialization of microinverters from 2010 to 2013. He joined the Department of Electrical and Computer Engineering, University of Alberta, Edmonton, Canada, in 2013.

Dr. Khajehoddin was an Associate Editor for the IEEE TRANSACTIONS ON SUSTAINABLE ENERGY from 2013 to 2021. He is currently an Associate Editor for the *Journal of Emerging and Selected Topics in Power Electronics* and IEEE TRANSACTIONS ON POWER ELECTRONICS

Javad Mashreghi received the Ph.D. degree in pure mathematics from McGill University, Montreal, QC, Canada, in 2001.

He is a Canadian mathematician and author working in the fields of functional analysis, operator theory and complex analysis. In particular, he is known for his contributions to analytic function spaces and operators acting on them.

Prof. Mashreghi was the 35th President of the Canadian Mathematical Society (CMS), is a Lifetime Fellow of CMS, and works as Professeur Titulaire at Université Laval. He is a Fellow Member of Canadian Mathematicians Society (CMS). He was awarded the G. de B. Robinson Prize of CMS in 2004 and the Khwarizmi International Award of IROST in 2009, which he declined. He is immensely involved in various aspects of North America's mathematical community, having served on numerous editorials, administrative and selection committees across Canada and the U.S. (CMS, AMS, Fields Institute, CRM, NSERC, NSF). He is the Editor-In-Chief of the Canadian Mathematical Bulletin (2020–2025) and Concrete Operators (2018–2022), and an Associate Editor of the Proceedings of The American Mathematical Society (2020–2024).

Khurram K. Afridi (Senior Member, IEEE) received the B.S. degree in electrical engineering from the California Institute of Technology (Caltech), Pasadena, CA, USA, in 1989, and the S.M. and Ph.D. degrees in electrical engineering and computer science from the Massachusetts Institute of Technology (MIT), MA, USA, in 1992 and 1998, respectively.

During summers and between degrees he worked for JPL, Lutron, Philips, and Schlumberger. In 1997, he was with the founding team of Techlogix as Chief Technology Officer and became Chief Operating Officer in 2000. From 2004 to 2008, he also led the development of LUMS School of Science and Engineering as Project Director, and was appointed Associate Professor and the Werner-von-Siemens Chair for Power Electronics in 2008. From 2009 to 2014, he was a Visiting Associate Professor in the Department of Electrical Engineering and Computer Science at MIT, and from 2014 to 2018, he was an Assistant Professor with the Department of Electrical, Computer and Energy Engineering, University of Colorado Boulder. Since August 2018, he is an Associate Professor in the School of Electrical and Computer Engineering at Cornell University. He is co-author of five IEEE prize papers. His research interests include power electronics and energy systems incorporating power electronic controls.

Prof. Afridi is an Associate Editor for the IEEE Journal of Emerging and Selected Topics in Power Electronics. He is a recipient of Caltech's Carnation Merit Award, CU Boulder's Goh Faculty Fellowship, the BMW Scientific Award, and the NSF CAREER Award.